A Model for Urban Biogenic CO_2 Fluxes: Solar-Induced Fluorescence for Modeling Urban biogenic Fluxes (SMUrF v1)

Dien Wu[1,*], John C. Lin[1], Henrique F. Duarte[1,‡], Vineet Yadav[2], Nicholas C. Parazoo[2], Tomohiro Oda[3,4,5], and Eric A. Kort[6]

5 [1]Department of Atmospheric Sciences, University of Utah, Salt Lake City, USA
[2]NASA Jet Propulsion Laboratory, California Institute of Technology, Pasadena, USA
[3]Goddard Earth Sciences Technology and Research, Universities Space Research Association, Columbia, USA
[4]Global Modeling and Assimilation Office, NASA Goddard Space Flight Center, Greenbelt, USA
[5]Department of Atmospheric and Oceanic Science, University of Maryland, College Park, USA
10 [6]Climate and Space Sciences and Engineering, University of Michigan, Ann Arbor, USA
[*]Now at Division of Geological and Planetary Sciences, California Institute of Technology, Pasadena, USA
[‡]Now at Earth System Science Center, National Institute for Space Research, São José dos Campos, Brazil

Correspondence to: Dien Wu (dienwu@caltech.edu)

Abstract. When estimating fossil fuel carbon dioxide (FFCO2) emissions from observed CO_2 concentrations, the accuracy can
15 be hampered by biogenic carbon exchanges during the growing season even for urban areas where strong fossil fuel emissions are found. While biogenic carbon fluxes have been studied extensively across natural vegetation types, biogenic carbon fluxes within an urban area have been challenging to quantify due to limited observations and differences between urban versus rural regions. Here we developed a simple model representation, i.e., Solar-Induced Fluorescence (SIF) for Modeling Urban biogenic Fluxes ("SMUrF"), that estimates the gross primary production (GPP) and ecosystem respiration (R_{eco}) over cities
20 around the globe. Specifically, we leveraged space-based SIF, machine learning, eddy-covariance (EC) flux data, and ancillary remote sensing-based products, and developed algorithms to gap fill fluxes for urban areas. Grid-level hourly mean net ecosystem exchange (NEE) are extracted from SMUrF and evaluated against 1) non-gapfilled measurements at 67 EC sites from FLUXNET during 2010 – 2014 (r > 0.7 for most data-rich biomes), 2) independent observations at two urban vegetation and two crop EC sites over Indianapolis from Aug 2017 to Dec 2018 (r = 0.75), and 3) an urban biospheric model based on
25 fine-grained land cover classification in Los Angeles (r = 0.83). Moreover, we compared SMUrF-based NEE with inventory-based FFCO2 emissions over 40 cities and addressed the urban-rural contrast in both the magnitude and timing of CO_2 fluxes. To illustrate the application of SMUrF, we used it to interpret a few summertime satellite tracks over four cities and compared the urban-rural gradient in column CO_2 (XCO2) anomalies due to NEE against XCO2 enhancements due to FFCO2 emissions. With rapid advances in space-based measurements and increased sampling of SIF and CO_2 measurements over urban areas,
30 SMUrF can be useful for informing the biogenic CO_2 fluxes over highly vegetated regions during the growing season.

1 Introduction

Climate change and urbanization are two major worldwide phenomena in recent decades. In close connection with both themes, cities have attracted increasing attention from both researchers and policymakers. Urban ecosystems are unique and complex given the wide variety of land use/covers in cities, along with higher levels of atmospheric CO_2 concentration, air temperature, and vapor pressure deficit than surrounding rural ecosystems (George et al., 2007). The consequences of climate change, such as severe heat, drought, and water shortage events, may be exacerbated particularly over (semi)arid and/or developing cities (Rosenzweig et al., 2018), resulting in possible population movement from increasingly hot/dry places to relatively cool/moist ones. Meanwhile, rapid urban expansion and population growth contribute to the rise in the total anthropogenic CO_2 emissions into the atmosphere and urban heat island that further influences the plant phenology (Meng et al., 2020). Human activities have been continuously modifying the urban and natural vegetation and soil, e.g., expansion of agricultural lands at the cost of the natural landscape, leading to less reversible ecological and climatic impacts (Ellis and Ramankutty, 2008; Hutyra et al., 2014; Pataki et al., 2006). Hence, urban areas function as both biophysical and socioeconomic systems, and studying their carbon sources/sinks facilitates understanding cities' roles in the global carbon cycle.

To study the urban carbon pool and its exchange with the atmosphere, the top-down approach based on measured atmospheric CO_2 concentrations is commonly used. McRae and Graedel (1979) noted over four decades ago that separation between anthropogenic and biogenic CO_2 flux signals is needed to interpret urban CO_2 observations. Biogenic CO_2 fluxes are found to modify the surface CO_2 and even atmospheric column CO_2 (XCO_2) concentrations downwind (e.g., Lin et al., 2004, Turnbull et al., 2015, Hardiman et al., 2017, Sargent et al., 2018, Ye et al., 2020). For example, the seasonal variation in biogenic CO_2 signals in Los Angeles was found to be one-third of the observed annual mean anthropogenic signal and further highlights the importance of urban irrigation (Miller et al., 2020). Over the Pearl River Delta in China, simulated biogenic contributions using 15 different models in the Multi-scale Synthesis and Terrestrial Model Intercomparison Project (MsTMIP, Huntzinger et al., 2013) lead to downwind XCO_2 anomalies ranging from nearly zero up to 1 ppm depending on seasons and models, which reveal the non-neglectable biogenic influence on XCO_2 as well as the large inter-model uncertainty (Ye et al., 2020). Thus, assessing the contributions from biogenic fluxes in observed signals is crucial for top-down estimates of urban emissions and yet remains challenging, especially given limited urban fluxes observations across the globe. Although deciduous trees are found to be the dominant tree type in urban areas based on a meta-analysis of 328 global cities (Yang et al., 2015a), a more accurate approximation of the vegetation coverages, types, and biological activities in cities is currently hard to obtain.

Existing approaches to separate biogenic and anthropogenic CO_2 components involve the use of ancillary tracers and terrestrial biospheric models. For instance, since radiocarbon (^{14}C) has decayed in fossil fuels, ^{14}C serves as a tracer for the combustion of FF emission (Miller et al., 2020; Turnbull et al., 2015). Carbonyl sulfide (COS) shares a similar seasonal variation as CO_2 over the land, a result of biospheric sinks (Kettle et al., 2002). However, measurements of ^{14}C, COS, and CO_2 fluxes are costly

and lacking in most cities around the globe. Besides observations, many global terrestrial biospheric models provide insights for informing and constraining CO_2 fluxes at continental to global scales (Huntzinger et al., 2013; Knorr and Heimann, 2001; Philip et al., 2019), but their relatively coarse resolution and simplifications on urban biosphere limit the use for studying urban carbon cycles. Only a few biospheric models are designed for simulating urban biogenic fluxes. Research has revealed urban-

5 rural differences in vegetation and soil properties, in part due to management strategies and environmental conditions, which complicate the flux quantification (Decina et al., 2016; Hardiman et al., 2017; Smith et al., 2019; Vasenev and Kuzyakov, 2018). Among these few models, the urban Vegetation Photosynthesis and Respiration Model (urbanVPRM, Hardiman et al., 2017) is an empirical model that incorporates the urban heat island effect and impervious surface area into its flux calculations and currently uses conventional greenness indices e.g., the Enhanced Vegetation Index (EVI).

Our work is primarily motivated by the relatively coarse spatial grid spacing and the simplifications of urban ecosystems in many models. We attempted to bridge between coarse-scale global biospheric models and highly customized local models to offer a global solution to modeling biogenic CO_2 fluxes within and around urban areas, which would provide insight into CO_2 partitioning between fossil fuel and biogenic components.

Thanks to advances in spaceborne and ground-based measurements, solar-induced fluorescence (SIF) has been retrieved successfully from various satellite platforms and has proven to be an effective proxy for photosynthesis and thus modeling gross primary production (GPP) (Frankenberg et al., 2011a; Guanter et al., 2014; Joiner et al., 2013; Yang et al., 2015b). SIF tracks the unique seasonal and interannual variations in GPP across diverse plant functional types (PFT) (Luus et al., 2017;

20 Smith et al., 2018; Turner et al., 2020; Zuromski et al., 2018) and their responses to physiological stress (Magney et al., 2019). In an effort to improve long-term, high resolution spatial mapping capabilities, several spatially continuous SIF products have been created using machine learning (ML) techniques and light use efficiency modeling to combine satellite retrieved SIF with ancillary vegetation data (Duveiller et al., 2020; Duveiller and Cescatti, 2016; Li and Xiao, 2019a; Turner et al., 2021; Zhang et al., 2018). Moreover, the empirical and PFT-specific linear correlations between GPP and SIF, derived from regressions of

25 temporally aggregated (~monthly) with eddy covariance GPP (Frankenberg et al., 2011; Guanter et al., 2014; Magney et al., 2019; Sun et al., 2017; Turner et al., 2021; Zhang et al., 2018; Zuromski et al., 2018) have spurred the development of upscaled GPP estimates (Li and Xiao, 2019b; Yin et al., 2020). SIF information has also been incorporated into existing process-based biospheric models and data assimilation systems (MacBean et al., 2018; Van Der Tol et al., 2009). Within the context of the urban biosphere, SIF retrieved from space has shown to reveal the urban-rural gradient in photosynthetic phenology (Wang et

30 al., 2019). Given all these advantages, SIF would potentially benefit the GPP estimates and CO_2 fluxes partitioning over cities.

Ecosystem respiration (R_{eco}), the other component of the net ecosystem exchange (NEE), is defined as the sum of the autotrophic (R_A) and heterotrophic (R_H) components. In terms of modeling urban R_{eco}, urbanVPRM follows the conventional approach of VPRM (Mahadevan et al., 2008) to estimate an initial air temperature (T_{air})-scaled R_{eco} and splits R_{eco} into equal

components (R_A and R_H) that will be further modified by considering impervious fractions and urban heat island effects (Hardiman et al., 2017). However, the exact partitioning of R_{eco} between R_A versus R_H and the separation between above- versus below-ground respiration can be challenging and highly uncertain, as acknowledged in Hardiman et al. (2017). The initial R_{eco} that urbanVPRM modified may be an overly simplistic function of ambient air temperature. After all, the complexity of biological and non-biological processes of R_{eco} and the lack of mechanistic understanding of how biotic and abiotic factors affect R_{eco} render challenging mechanistic modeling of R_{eco}. Given the complexity in modeling R_{eco}, we will turn instead to ML techniques that have been increasingly applied in many disciplines to help answer complicated, entangled problems via extracting patterns from data streams for predictions and generalizations. Reichstein et al. (2019) provided a comprehensive review on the many applications of ML techniques in solving geoscience and remote sensing problems and identified challenges in successfully adopting ML approaches—e.g., interpretability, integration with physical understanding and modeling, and the ability to cope with model/data uncertainties. In the context of ecosystem modeling, artificial neural network (NN) has been utilized to generate SIF beyond satellite soundings (Li and Xiao, 2019a; Zhang et al., 2018), harmonize multiple SIF satellite instruments (Wen et al., 2020), map carbon and energy fluxes (Tramontana et al., 2016), and reveal and predict the trend in global soil respiration (Zhao et al., 2017).

In this paper, we present a model representation of GPP, R_{eco}, and NEE fluxes targeting urban areas around the globe, the *Solar-Induced Fluorescence (SIF) for Modeling Urban biogenic Fluxes* ("SMUrF"), by taking advantages of SIF and NN technique. Our main objectives include: 1) examine the biogenic and anthropogenic CO_2 fluxes and their temporal variations over urban and surrounding rural areas; and 2) demonstrate one application of SMUrF to help interpret satellite CO_2 observations by revealing the urban-rural gradient in biogenic CO_2 fluxes along satellite swaths of the Orbiting Carbon Observatory 2 (OCO-2, Crisp et al., 2012).

2 Data and methodology

SMUrF incorporates SIF as an indicator of photosynthesis, along with possible drivers for R_{eco} (i.e., air and soil temperatures and SIF-driven GPP), and performs hourly downscaling using reanalysis-based temperature and radiation fields (**Fig. 1**). We accounted for variations in biome types and R_{eco} at 500 m before aggregating fluxes to the final grid spacing of 0.05°. Gridded uncertainties of daily mean fluxes are quantified by assigning biome-specific coefficient of variations (CVs) from model-data comparisons (**Sect. 2.5**). To gain insight into the column CO_2 anomalies caused by anthropogenic and biogenic fluxes, we further adopted an atmospheric transport model to link fluxes and concentrations (**Sect. 2.6**). Before introducing the steps for estimating individual flux components, we first go through the main input datasets (**Sect 2.1**).

2.1 Input datasets

Similar to many biospheric models, SMUrF estimates gridded GPP, R_{eco}, and NEE (= R_{eco} – GPP) fluxes based on land cover types. Main required data streams are summarized in **Fig. 1**, including 1) the 500 m MODIS-based land cover classification; 2) 0.05° spatiotemporally contiguous SIF (CSIF) product; 3) 100 m above-ground biomass (AGB) from GlobBiomass; 4) eddy-covariance (EC) flux measurements across continents; and 5) gridded products of air and soil temperatures.

2.1.1 Land cover classification

Land cover classifications with more sophisticated algorithms in urban areas (e.g., NLCD 2016) are often available for limited regions. Thus, we adopted the land cover types defined by the International Geosphere–Biosphere Programme (IGBP) from MCD12Q1 v006 (Friedl and Sulla-Menashe, 2019) to inform biome types over global lands. Twelve biomes include croplands (CRO), closed and open shrublands (CSHR, OSHR), deciduous/evergreen broadleaf/needleleaf forests (DBF, DNF, EBF, ENF), grasslands (GRA), mixed forests (MF), savannas (SAV), woody savannas (WSAV), and permanent wetlands (WET). Since MCD12Q1 simply treats the entire urban area as one category (URB), we developed an algorithm to approximate the vegetation types and fractions in cities (**Sect 2.2.2**).

2.1.2 Data for GPP estimates

We used spatiotemporally Contiguous SIF (CSIF, Zhang et al. 2018) product and GPP fluxes from FLUXNET2015 (Pastorello et al., 2017) to calculate biome-specific GPP-CSIF slopes (α, **Supplementary Fig. S1**). 98 global EC tower sites with screened data points (quality flag < 3) from 2010 to 2014 are chosen to represent various biomes. CSIF offers global 4-day mean SIF at the grid spacing of 0.05° during 2000–2018 using the NN approach (Zhang et al., 2018). The NN model in CSIF is constructed based upon OCO-2 SIF and four broadband reflectances from MCD43C4 V006 under clear-sky conditions and is used for mapping SIF beyond sounding locations. CSIF agrees well with SIF retrievals from OCO-2 and GOME-2, considering the inevitable spatial mismatch between CSIF (0.05°) and the direct sounding-level SIF measurements (OCO-2's footprint of ~1 km × 2 km). Two largest biases of CSIF with respect to OCO-2 SIF arise from croplands (–12.72 %) and urban areas (–14.59 %), caused by the saturation effect in broadband reflectances and built-up contaminations to the reflectance signal, respectively (Zhang et al., 2018). To compensate for the potential bias of urban CSIF, we scale up the GPP-SIF slope for urban areas (details in **Sect. 2.2.2**).

In addition, the clear-sky instantaneous CSIF are compared to TROPOMI-based downscaled SIF for summer 2018 (Turner et al., 2021) and vegetated fractions inferred from the WUDAPT product (**Appendix A**). Despite some discrepancies over a few regions, these comparisons confirmed CSIF's performance and capability in revealing urban-rural gradient in biogenic activities (**Supplementary Figs. S2-S3**).

2.1.3 Data for approximation of urban vegetation globally

To assign trees and grass within the MODIS-based urban domain, several steps are carried out to approximate the relative fractions of 1) tree versus non-tree, 2) individual tree types, and 3) grassland versus shrubland (details in **Sect. 2.2.2**). Relative tree fractions (i.e., ratio of tree fractions to total vegetated fractions) can be obtained from two data sources—i.e., a 0.6 m NAIP-based urban land cover product (Coleman et al. 2020) and a 250 m Vegetation Continuous Fields (VCF) from MOD44B (Dimiceli et al., 2015). Both products offer estimated tree and vegetated fractions. The former one is produced only over Los Angeles via random forest algorithms that trained on Sentinel-2 (~5 m) and NAIP (~0.6 m) optical imagery (Coleman et al., 2020) and possesses much higher tree fractions than MODIS VCF (see comparisons in **Sect. 2.2.2**). Thus, we decided not to utilize MODIS VCF for indicating urban vegetation in this work, only for comparing tree fractions from Coleman et al. (2020).

To approximate relative tree fractions (f_{tree}) in cities, we treat the gridded AGB at 100 m from GlobBiomass (Santoro et al. 2018) as the spatial proxy (see methodology explained in **Sect. 2.2.2**). GlobBiomass deployed a complex retrieval algorithm system which involves a series of retrieval algorithms using the radar backscatter and several other data such as laser measurement from ICESAT (Schutz et al., 2005), the tree and land cover data (e.g., from Landsat), and collections of reanalysis and models. AGB and its grid-level uncertainty [tons ha^{-1}] by definition describe the "oven-dry weight of the woody parts (stem, bark, branches, and twigs) of all living trees excluding stump and roots" (Santoro et al. 2018). GlobBiomass AGB has demonstrated good agreement against independent data products for different continents (Santoro et al. 2018).

2.1.4 Reanalyses for R_{eco} estimates

In efforts to train and predict R_{eco} via neural network models, we chose GPP, air and soil temperatures (T_{air} and T_{soil}) as explanatory variables (details in **Sect. 2.3**). Modeled T_{air} and T_{soil} are grabbed from the ECMWF ReAnalysis-5 (ERA5, 0.25°; Copernicus Climate Change Service Information, 2017) for the entire globe; or from Daymet (1km; Thornton et al., 2016) and the North American Land Data Assimilation System (NLDAS, 0.125°; Xia et al. 2012) as alternative inputs for CONUS runs (**Fig. 1**). It is worth pointing out that different models/reanalysis provide T_{air} at 2 meters above ground but T_{soil} at different soil depths. For instance, four soil depths from NLDAS range from 10, 30, 60, and 100 cm below ground, whereas ERA5 simulates mean T_{soil} over four vertical layers, i.e., 0 – 7, 7 – 28, 28 – 100, and 100 – 289 cm. Measured soil depths from FLUXNET are even more complicated and vary among sites with the most common shallowest soil depth of ~2 cm below ground. To reconcile differences in soil depths, we chose measured T_{soil} from the shallowest layer in both the model and observational datasets and separately build NN models (**Sect. 2.3**).

2.1.5 Data for flux comparisons

We further carried out flux comparisons against two independent sets of eddy-covariance data, i.e., FLUXNET2015 and the Indianapolis Flux Experiment (INFLUX; Davis et al., 2017, Wu et al., 2020a), and one alternative urban biospheric model of

urbanVPRM over Los Angeles in **Sect. 3.2**. Only non-gapfilled measured NEE fluxes from FLUXNET2015 (with quality flag of 0) are used for validation. Since NEE fluxes measured from INFLUX have not been gap-filled, we only chose the hours from SMUrF where valid INFLUX data are available.

5   The INFLUX project includes EC flux measurements which accompany the tower- and aircraft-based GHG mole fraction measurements. These sites have been periodically moved to sample different components of the urban landscape. For the period from Aug 10, 2017 to June 7, 2019, these flux towers were deployed at two urban vegetation sites (#1 and #4) and two agricultural sites (#2 and #3). Two urban vegetation (turf grass) sites were located in a cemetery area (site #1) and a golf course (site #4). Because CSIF is not available beyond 2018 as of this writing, we cannot yet extend the flux comparison into 2019.

10   Fluxes from INFLUX sites were computed using EddyPro software (LI-Cor, Inc., Lincoln, NE; Biosciences, 2012, 2017) and post-processed to filter out data when a) the LI-COR gas analyser signal strength was low and b) during periods of weak turbulence (Wu et al., 2020a). It is worth noting that INFLUX data provides valuable independent evaluations as flux sites with urban imprint are lacking from FLUXNET2015 and observed fluxes from INFLUX sites were not used when calibrating parameters in SMUrF.

The urbanVPRM model, applied over Los Angeles, estimates GPP from a light use efficiency modeling perspective driven by reanalysis-based Photosynthetically Active Radiation (PAR) and satellite-derived EVI and Land Surface Water Index for phenology and water availability; and estimates R_{eco} via an air temperature function with extra modifications to air temperature due to urban heat island effect and impervious surface area. UrbanVPRM-based fluxes rely on the 60 cm NAIP-based land

20   cover classification in Los Angeles (Coleman et al., 2020; **Sect. 2.1.3**). Due to differences in grid spacing between models, fluxes from urbanVPRM are aggregated and re-projected from 30 m to 0.05° to match SMUrF for purposes of comparison.

2.2 GPP estimates

We used 4-day mean clear-sky SIF from CSIF and 4-day mean observed GPP fluxes from 98 global eddy-covariance (EC) towers from FLUXNET2015 to derive biome-specific GPP-SIF slopes (α, **Supplementary Fig. S1**) with special treatments

25   to α over croplands and urban areas described in the following subsections. While non-linear relationships between SIF and GPP at leaf- and canopy- level have been observed (Helm et al., 2020; Magney et al., 2017; Maguire et al., 2020; Marrs et al., 2020; Verma et al., 2017), GPP is observed to be linearly related to SIF at increasing temporal and spatial (ecosystem and regional) scales (Frankenberg et al., 2011; Sun et al., 2017) as leaf-level differences in composition, light exposure, stress, and stress response mix out (Magney et al., 2020). Considering uncertainty in CSIF and flux tower-partitioned GPP as well as the

30   noise in the GPP-SIF relationship across global flux sites (**Supplementary Fig. S1**), we adopted linear fits instead of non-linear fits between GPP and CSIF. Errors due to departure from linearity will be implicitly included in GPP uncertainties calculated from model-tower validations (**Sect. 2.5**). The calculated α values are in proximity to those reported in Zhang et al. (2018) from 40 towers and are then assigned to each 500 m gridcell according to its corresponding biome type.

2.2.1 C3/C4 partitioning of croplands

GPP-SIF relationships differ between C4 and C3 crops at the canopy scale, since GPP for C3 crops may saturate at high PAR levels. Different statistical fits between observed GPP and SIF are suggested in use for C3 versus C4 crops (He et al., 2020). Despite the focus of SMUrF on urban areas, we still attempted to differentiate C4 from C3 crops and estimate two different α values from EC sites dominated by C3 or C4 crops. Specifically, the Spatial Production Allocation Model (SPAM 2010V1.1, You et al., 2014) is used for areal estimates of 42 crop species, among which the following are identified as C4 crops: maize, pearl and small millet, sorghum, and sugarcane. As a result, we produced maps of C3:C4 ratios at a grid spacing of 10 km for the entire world (**Fig. 2ab**). Four of the selected 13 cropland EC FLUXNET sites fall within grid cells with high C4 ratio of > 50%; the remaining sites fall into grid cells with C4 ratios of < 10%. We thereby arrive at α_{C4} of ~35.6 [μmol m^{-2} s^{-1}]:[mW m^{-2} nm^{-1} sr^{-1}] from sites with high C4 ratio and α_{C3} of ~19.7 [μmol m^{-2} s^{-1}]:[mW m^{-2} nm^{-1} sr^{-1}] from the rest 9 cropland sites. Eventually, we calculated the weighted mean α according to the C3:C4 ratio map and identified tropical regions, mid-west US, northeastern China, and spots in India and south Africa as regions with higher α and C4 crop ratios (**Fig. 2c**). Note that these weighted mean α will only be activated over MODIS-based croplands.

2.2.2 Modification to urban vegetation

We next turn to the estimate of α over MODIS-based "urban" category shown in the following three steps (**Fig. 1**):

1) *Estimate the relative tree fraction (f_{tree} = tree / vegetated).* A power-law relationship (**Fig. 3a**) between AGB bins and relative tree fractions obtained from the NAIP-based land cover classification (top panel in **Fig. 3b**) is used to predict f_{tree} (bottom panel in **Fig. 3b**). Although the AGB binning procedure may not fully recreate the variations in f_{tree} especially for grid cells with zero AGB (dark red hexagons in **Fig. 3a**), the predicted f_{tree} using AGB is tied to a smaller bias of +2.3 % than f_{tree} using MOD44B (–23.5 %), when the high-resolution NAIP-based land cover product is compared (**Fig. 3b**).

2) *Estimate relative fractions of five tree types, grass, and shrub based on climatology.* Due to the lack of global data on urban biome types, the relative non-tree vegetated fraction ($f_{non-tree}$ = $1 - f_{tree}$) is simply split into half grass and half shrub (2nd row in **Fig. 4**). The relative tree fractions are divided into five possible tree types (i.e., DBF, DNF, EBF, ENF, MF). The share of each tree type in cities is approximated as a function of latitude based on the climatology of land cover types (**Supplementary Fig. S4a**) — e.g., high fractions of ENF over high-latitudes, EBF over tropical lands, and DBF plus MF over the midlatitudes (**Supplementary Fig. S4b**).

3) *Calculate weighted mean α.* α for urban areas are weighted mean values calculated from biome-specific α values and their corresponding fractions approximated in step 2. To account for potential negative bias of ~14.5% in CSIF over cities (Zhang et al., 2018), we scaled up urban α by 1.145.

In the end, α at 500 m over urban and natural lands (3rd row in **Fig. 4**) are aggregated to 0.05° and multiplied by CSIF to arrive at GPP at 0.05°. The exact partitioning between grass and shrub in step 2) plays a minor role on the final GPP flux at 0.05° (**Supplementary Fig. S5**). It is worth clarifying that we implicitly assumed vegetation "exists" over urban grid cells and only solved for the relative tree/grass fractions as illustrated in steps 1) and 2), as information of vegetated/impervious fractions has been embedded in the CSIF product. Additional information about vegetated/impervious fractions was not necessary in the calculation of α for every 500 m urban grid (see **Appendix A** for more explanations).

2.3 R_eco estimates

Three explanatory variables—T_{air}, T_{soil}, and GPP— are chosen to train against the observed daily mean R_{eco} from FLUXNET. To account for mismatches in reported soil depths (introduced in **Sect. 2.1.4**), we built separate sets of NN models using 1) direct temperatures and GPP observations from EC towers, 2) ERA5-based temperatures and SIF-based GPP, or 3) Daymet & NLDAS-based temperatures and SIF-based GPP (only for US as alternative runs). SIF-based GPP is ingested in order to pass SIF information onto R_{eco} estimation. Data points from a few EC sites with relatively large uncertainties in modeled GPP were excluded before the training of NN models to prevent error propagation into R_{eco} (**Appendix B**).

For each set of NN model, we manually split data points based on their biome types and obtain 12 separate NN models. Data points from open and closed shrublands are combined due to the extremely low numbers of EC sites around the globe. To be consistent with the C3:C4 crops partition for GPP estimates (**Sect. 2.2.1**), we obtained 2 separate NN models for C3 and C4 crops and calculated the weighted mean R_{eco} based on the derived C3:C4 ratios. 80 % and 20 % of the data points per biome are used for training and testing, respectively. Models with two hidden layers are constructed with 32 and 16 neurons chosen for the first and the second layer. We computed R_{eco} at 500 m by applying biome-specific models and aggregated those R_{eco} to 0.05°. We also tested two alternative ways to train R_{eco} based on 1) all data points without differentiating their land cover types and 2) additional categorical variables from biomes and month and season of the year. Please refer to **Appendix B** for sensitivity tests and technical details about data preparation and cross validation of neural networks.

2.4 NEE estimates

We obtained hourly surface downward shortwave radiation (SW_{rad}) and air temperature (T_{air}) from the ERA5 reanalysis to calculate the hourly scaling factors for GPP and R_{eco}. T_{air} and SW_{rad} are initially provided on a grid spacing of 0.25° and then bilinearly interpolated to 0.05°. To estimate the hourly radiation scaling factors I_{scale} for GPP, we normalized the hourly SW_{rad} by the 4-day mean SW_{rad} with the same time window of the 4-day mean GPP. Regarding the calculation of hourly temperature scaling factors T_{scale} for R_{eco}, a temperature sensitivity function (SR_{1h}) has been modified from prior studies (Fisher et al., 2016; Olsen and Randerson, 2004):

$$SR_{1h} = Q_{10}^{\frac{T_{air,1h}-30°C}{10°C}}, \tag{1}$$

where Q_{10} is an unitless temperature sensitivity parameter that could vary across biomes and T_{air} is in °C. Because the hourly downscaling procedure is performed on GPP and R_{eco} fluxes at 0.05° and no single biome is tied to each 0.05° grid cell, we adopt a typical Q_{10} value of 1.5 according to previous studies (Fisher et al., 2016) despite possible biome-dependent variations in Q_{10}. SR_{1h} is then normalized by its daily mean value to obtain T_{scale}. Finally, T_{scale} and I_{scale} are used to temporally downscale the daily mean R_{eco} and 4-day mean GPP, i.e., $\overline{R_{eco,1d}}$ and $\overline{GPP_{4d}}$:

$$R_{eco,1h} = \overline{R_{eco,1d}} * T_{scale} = \overline{R_{eco,1d}} * \frac{SR_{1h}}{\frac{1}{24}\Sigma_{1d} SR_{1h}},$$

$$GPP_{1h} = \overline{GPP_{4d}} * I_{scale} = \overline{GPP_{4d}} * \frac{SW_{rad,1h}}{\frac{1}{24*4}\Sigma_{4d} SW_{rad,1h}}. \tag{2}$$

Examples of I_{scale} and T_{scale} over the western US on July 2, 2018 are displayed in **Supplementary Fig. S6bc**. As a sanity check for the ERA-based SW_{rad}, a higher resolution product is utilized, of which SW_{rad} and PAR were estimated based on the Earth Polychromatic Imaging Camera (EPIC) data onboard the Deep Space Climate Observatory (DSCOVR) and random forest algorithms (Hao et al., 2020a, 2020b). The EPIC-based radiation data is available globally at 10 km from June 2015 to June 2019 and has been validated against in situ observations from the Baseline Surface Radiation Network and Surface Radiation Budget Network. Hourly I_{scale} using ERA5-based SW_{rad} and EPIC-based SW_{rad} or PAR generally agree well regarding the diurnal cycles, despite small discrepancies in peak radiation and I_{scale} values during noon hours (**Supplementary Fig. S6de**).

2.5 Uncertainty quantification and direct flux validation

Error quantification is important for characterizing the precision and accuracy of modeled fluxes. Previous studies have carried out comprehensive uncertainty estimates towards their reported biogenic flux estimates (Dietze et al., 2011; Hilton et al., 2014; Lin et al., 2011; Xiao et al., 2014). Here we estimated errors in modeled GPP and R_{eco} based on FLUXNET observations.

We extrapolated the biome type, 4-day mean SIF, and daily mean T_{air} & T_{soil}, from their originated gridded fields to each flux tower location and computed directly the modeled GPP and R_{eco} using α value and NN models. Comparisons between these direct computations and screened observations from FLUXNET2015 yield biome-specific root-mean-square errors (RMSE), mean biases, and coefficient of variations (CV). The uncertainties in assuming linear GPP-SIF relationship were not explicitly quantified but incorporated within these error statistics on top of other error sources such as inter-site variations. Eventually, biome-specific CVs are assigned to each 500 m grid and aggregated to 0.05° assuming statistical independence. For visualization purpose, we collected model-data pairs regardless of their biome types as density plots in **Fig. 5**.

Directly computed 4-day mean GPP at most towers match well with observations regarding their magnitude and seasonality. Modeled GPP shows underestimations against irrigated maize sites in Nebraska (e.g., US-Ne1, US-Ne2) and sites in the central valley (e.g., US-Twt) in California (**Supplementary Fig. S8**) likely because irrigation effect is not implicitly included, and high crop chlorophyll concentration may not be fully recreated in the reflectance-driven CSIF data. Nevertheless, the overall

correlation coefficient between directly modeled GPP and partitioned GPP from FLUXNET is 0.86 with a mean bias of –0.069 μmol m^{-2} s^{-1} for 89 tower sites. When removing cropland sites from consideration, RMSE in 4-day mean GPP drops from 1.91 to 1.74 μmol m^{-2} s^{-1} (**Fig. 5a** vs. **5b**).

5 Next, we reported the predicting performance of R$_{eco}$ only using testing sets, i.e., 20 % of the entire data volume. R$_{eco}$ trained and predicted using measured variables from FLUXNET overperform the ones using ERA5's temperatures and SIF-modeled GPP (r = 0.90 vs. r = 0.87; **Fig. 5c** vs. **5d**). The constant CSIF within a 4-day interval and the constant α over seasons make it difficult to reproduce daily variations in R$_{eco}$ as T$_{air}$ and T$_{soil}$ likely become the main drivers. Recall that temperature fields from higher resolution fields of Daymet + NLDAS were also used for training and predicting R$_{eco}$ over CONUS. These Daymet

10 + NLDAS runs appear to slightly outperform the ERA5 runs (**Fig. 5g** vs. **Fig. 5f**). Although the NN model using observed variables yields the best performance, we are inclined to use NN models trained by modeled features for two reasons: 1) to account for discrepancies in GPP and temperature between tower observations and model/reanalyses and 2) for spatial generalization beyond points with "ground truth" as only modeled GPP are available away from the EC sites. Nevertheless, mean bias on testing sets across biomes remains small (< 10^{-3} μmol m^{-2} s^{-1}) with RMSE of 1.14 μmol m^{-2} s^{-1}. Since the error

15 statistics associated with the ERA5 runs resemble those with the Daymet + NLDAS runs over the US (**Figs. 5f** vs. **5g**), we only present the ERA5-based results in the following sections.

An additional hourly mean NEE evaluation against FLUXNET can be found in **Sect. 3.2.1** and **Fig. 9**. We stress that the directly computed fluxes and the validation with FLUXNET presented in this section differ from those presented in **Sect. 3.2.1**,

20 as the latter one uses the spatially weighted mean flux at 0.05° that takes the spatial heterogeneity into account.

2.6 Comparisons of FFCO$_2$ vs. NEE fluxes and their contributions in column CO$_2$

FFCO$_2$ emissions from the Open-Data Inventory for Anthropogenic Carbon dioxide (ODIAC2019, Oda et al. 2018) are compared against NEE from SMUrF in terms of the seasonal magnitude, summertime diurnal cycle, and spatial distribution (**Sect. 3.1**). Initial ODIAC emissions at 1 km grid spacing are averaged to 0.05° for such FFCO$_2$-NEE comparisons. Although

25 the city-wide FFCO$_2$ emissions from ODIAC may differ from other reported emissions (Chen et al., 2020; Oda et al., 2019), ODIAC is widely used in many urban studies and provides sufficient insights to FFCO$_2$ emissions from a global perspective.

To further translate CO$_2$ fluxes into changes in column-averaged CO$_2$ concentrations, or XCO$_2$ (**Sect. 3.3**), we made use of an atmospheric transport model—i.e., the column version of the Stochastic Time-Inverted Lagrangian Transport (X-STILT, Wu

30 et al., 2018) model. We carried out four case studies by examining summertime OCO-2 tracks over Boston, Indianapolis, Salt Lake City, and Rome. Those 4 cities are chosen based on satellite data availability/quality and various vegetation coverages. Specifically, thousands of air parcels are released in STILT (Fasoli et al., 2018; Lin et al., 2003) from the same atmospheric columns as the OCO-2 soundings and driven by meteorological fields, i.e., the 3-km High Resolution Rapid Refresh (HRRR)

for US cities and 0.5° GDAS for non-US cities (Rolph et al. 2017). The X-STILT model returns hourly surface influence matrices or "column footprints" [ppm / (μmol m^{-2} s^{-1})] that incorporates the averaging kernel and pressure weighting profiles from OCO-2. The hourly footprints indicate the influence of each upwind gridcell onto downwind satellite soundings within each hour interval. The coupling between column footprints and surface fluxes, e.g., hourly SMUrF-based NEE or ODIAC-based FFCO$_2$ emissions, reveals 1) the spatially-explicit XCO$_2$ contribution [ppm] due to biogenic/anthropogenic fluxes and 2) the overall XCO$_2$ anomalies (XCO$_{2.bio}$, XCO$_{2.ff}$) at each receptor if aforementioned spatial contributions are summed up. For more details of ODIAC and X-STILT, please refer to Oda et al. (2018) and Wu et al. (2018), respectively.

3 Results

We start with modeled biogenic and anthropogenic fluxes at the regional and urban scales (**Sect. 3.1**) and their comparisons against EC observations and urbanVPRM over natural biomes and urban areas (**Sect. 3.2**). For the purpose of this paper gridded fluxes were produced from Jan 1, 2017 to Dec 31, 2018 only for the following populated/vegetated regions: CONUS, western Europe, east Asia, south America, central Africa, and eastern Australia.

3.1 Biogenic and anthropogenic CO$_2$ fluxes at the regional and city scale

To reveal the role of biospheric fluxes in the context of anthropogenic emissions, we summed up NEE from SMUrF and FFCO$_2$ emissions from ODIAC for each season over CONUS, western Europe and east Asia (**Fig. 6abc**). SMUrF reveals the spatial contrasts and seasonal variations in NEE fluxes, as informed by the use of SIF, land cover types, and temperature fields. Places with strong seasonal amplitude are found to be rural regions covered by crops and dense forests, e.g., eastern US, northeastern and southern China, and spotty locations over Europe (green shading areas in **Fig. 6abc**). After adding FFCO$_2$ emissions, the sum of NEE and FFCO$_2$ remain positive over east Asia even in summer months ("brownish" spots in **Fig. 6c**).

We next zoom into fluxes at the city-scale. SMUrF captures the increasing biospheric activities from urban cores to their rural surroundings inferred by Gross Ecosystem Exchange (GEE = -GPP), R$_{eco}$, and NEE components (eight zoomed-in panels in **Fig. 6**), as cities are usually associated with less vegetation coverage than their rural counterparts. The urban-rural difference in GEE over Salt Lake City, Boston, and Seoul is relatively small, in contrast to cities like Guangzhou and Tokyo. Since modeled R$_{eco}$ is partially driven by SIF-based GPP, the spatial variations of GEE and R$_{eco}$ appear alike to some extent. Even though GPP can be high over JJA 2018, summertime mean NEE remains small at urban cores, with values ranging from –1 to –2 μmol m^{-2} s^{-1}. For Boston, spatial distribution of GEE and R$_{eco}$ derived from SMUrF (**Fig. 6**) resemble what were reported using urbanVPRM (Fig. 2C in Hardiman et al., 2017). R$_{eco}$ from SMUrF exceed the ODIAC-based FFCO$_2$ emission over residential and rural areas away from the urban cores (**Fig. 6**), which coincides with Decina et al. (2016) that reported elevated rate of soil respiration approaching FFCO$_2$ emission in the residential area and forest to the west of the urban core. Yet, when it comes to interpreting observed CO$_2$ concentrations, it is the net flux that should better be compared against FFCO$_2$. In short,

biogenic fluxes have the potential to dominate the overall carbon flux exchange over residential/rural areas, while FFCO$_2$ is the main controller within urban cores.

We further extend the analysis to 40 cities across multiple continents to see how CO$_2$ fluxes vary between 1) urban vs. adjacent
5   rural areas, 2) different cities, 3) the FF vs. NEE components, and 4) across seasons. Specifically, FFCO$_2$ and NEE fluxes are averaged over "urban" and "rural" grid cells within a 2° × 2° region around city centers. Here "urban" grids are simply defined as the "urban and build-up settlements" according to MCD12Q1, while "rural" grids contain all the natural counterparts (e.g., forests, grasslands, croplands) except for water, ice, and barren lands. In particular, we are interested in the seasonal variation (**Sect. 3.1.1**) and mean summertime diurnal cycle (**Sect. 3.1.2**) of these "urban" and "rural" fluxes. The diurnal cycles of FFCO$_2$
10 are calculated using hourly scaling factors from Temporal Improvements for Modeling Emissions by Scaling (TIMES, Nassar et al., 2013) on top of monthly mean ODIAC-derived emissions. Note that emission temporal patterns provided by TIMES are climatological, based on a U.S gridded inventory by Gurney et al (2009), and thus do not change in response to local environmental conditions, such as air temperature.

3.1.1 Seasonal variation

15 Stronger net biospheric uptake during growing seasons and larger seasonal amplitude in NEE are linked to rural grids than to urban grids as expected (**Fig. 7a** vs. **7b**). Among the selected 40 cities, top "wet", biologically active cities include Boston, Baltimore-DC, New York, Taipei, London, Paris, and Rio de Janeiro. By contrast, a few "drier" cities stand out, with the spatially-average NEE over urban grids close to zero, such as Los Angeles, Phoenix, and Madrid (**Fig. 7a**). Besides NEE magnitude, cities reach their maximum net uptake at different times — e.g., June/July for most cities in eastern US and east
20 Asia (except for Taipei); a slight earlier peak for most cities in western US, western Europe, and Taipei; and January for cities in southern hemisphere. For instance, minimum NEE is found in late May to June within and around London (**Fig. 7a5**), which is consistent with the seasonality of the posterior NEE fluxes reported for UK from 2013 to 2014 (White et al., 2019).

Since FFCO$_2$ emission fluctuates less across seasons than NEE, we compare the magnitude of the seasonal amplitude in NEE
25 relative to the annual mean FFCO$_2$ emission (shown as numbers below city names in **Fig. 7**). Such comparison helps inform the potential interference from the biosphere over cities when interpreting long-term CO$_2$ observations, albeit without considering the atmospheric transport and that the one single number for FFCO$_2$ can be affected by large point source emissions. As expected, most spatially-average FFCO$_2$ emissions over urban grids are stronger than the seasonal amplitude in NEE (**Fig. 7a**). Exceptions include Pyongyang and cities in central Africa whose seasonal NEE amplitudes approach their annual mean
30 FFCO$_2$ emissions, e.g., 2.0 vs. 2.5 μmol m^{-2} s^{-1} for Lagos. Things can get more complex if one tries to interpret FFCO$_2$ signals from year-long observations over rural areas. Annual mean FFCO$_2$ emissions for rural grids seldom exceed 2 μmol m^{-2} s^{-1}, whereas seasonal amplitudes in the 4-day mean NEE often exceed 4 μmol m^{-2} s^{-1} (**Fig. 7b**) with a few exceptions in east Asia.

3.1.2 Diurnal cycle

In regard to the magnitude of hourly fluxes, FFCO$_2$ emissions is negligible for rural grids (**Fig. 8b**). Intensive FFCO$_2$ emissions ranging from 20 to 60 μmol m^{-2} s^{-1} dominate the total CO$_2$ fluxes even during noon hours for east Asian cities (**Fig. 8a3-4**). The urban biosphere over a few cities in eastern US and Europe may take up a considerable amount of CO$_2$, approaching or even exceeding FFCO$_2$ emissions during noon hours in summer months. For instance, the peak value in summertime average NEE and FFCO$_2$ fluxes over Boston is about –16 μmol m^{-2} s^{-1} and 10 μmol m^{-2} s^{-1} at the hourly scale, respectively (**Fig. 8a1**).

In regard to the timing of hourly fluxes, NEE in most mid-latitude cities start to dip below zero at 7 or 8 am local time (**Fig. 8a**), slightly later than the typical summertime sunrise hour of ~6 am, with a lag associated with the time it takes for GPP to offset R$_{eco}$. NEE reaches its minimum at different hours spanning from 11 am to 1 pm among cities and rises back to zero at or before 6 pm. On the contrary, FFCO$_2$ emissions start to rise largely due to morning traffic, stay elevated during daytime, and gradually declined between 8-9 pm. As for Boston, SMUrF reported similar NEE magnitude compared to urbanVPRM but with an hour delay where NEE becomes negative (**Supplementary Fig. S9** vs. Figure 3B3 in Hardiman et al., 2017), likely due to discrepancies in the hourly data that drive the hourly GPP fluxes.

3.2 Hourly flux comparisons

In this section, we will see how robust the modeled fluxes are at the hourly scale (**Sect. 3.2.1 – 3.2.2**) and how CO$_2$ fluxes impact the CO$_2$ concentrations downstream after considering atmospheric transport (**Sect. 3.3**). Specifically, simulated hourly mean NEE fluxes are extracted from the final gridded output fields and compared against measured NEE at EC sites from FLUXNET and INFLUX, which differ from the model-data comparison using directly computed daily fluxes in **Sect. 2.5**.

3.2.1 SMUrF vs. FLUXNET and INFLUX

We first evaluate modeled NEE against 67 EC tower sites from FLUXNET2015 in North America and Europe from 2010 to 2014 (**Fig. 9**). The correlation coefficient between simulated and measured hourly NEE ranges from 0.66 to 0.79 for most biome types, except for open shrubland likely due to limited amounts of data. Higher random and systematic uncertainties are associated with these hourly flux comparisons than direct daily validations shown in **Sect. 2.5** (**Fig. 5**), given larger flux magnitude along with errors propagated from GPP, R$_{eco}$ and hourly downscaling. The mean bias of hourly NEE ranges from –1.51 μmol m^{-2} s^{-1} for grassland to +1.11 μmol m^{-2} s^{-1} for closed shrubland. Croplands are associated with the highest RMSE, which stem from their large flux magnitudes and inter-site variations in GPP-CSIF relationships (**Supplementary Fig. S1**). The potential underestimation in 4-day average GPP over irrigated maize sites (e.g., US-Ne* as mentioned in **Sect. 2.5**) appears to be propagated into the NEE estimate (**Supplementary Fig. S10a**). Yet, if all sites with the same biome are treated together, the timing and magnitude of the 3-month mean diurnal cycle of NEE from SMUrF resemble those from FLUXNET

(**Supplementary Fig. S10b**). Since each 0.05° model grid is possibly comprised of various biome types, areal fractions of the specific biome indicated by each EC site over the 0.05° model grid is provided as a reference in **Supplementary Fig. S11.**

More importantly, we carried out independent NEE comparisons that leveraged four valuable EC sites from the INFLUX network over Indianapolis (**Fig. 10a, Sect. 2.1.5**). In 2018, observations at site #3 were affected by corn; while observations at site #2 were primarily influenced by soybean, although site #2 was surrounded by mixed crops of soybean and corn. As a result, site #3 shows a stronger observed uptake from mid-June to mid-July than site #2 (**Figs. 10c**), because corn is often associated with higher light saturation points and lower light compensation points, leading to higher light use efficiency and GPP than soybean. Although C3:C4 fractional contribution was incorporated into the calculation of α (**Sect. 2.2.1**), SMUrF is unable to differentiate NEE at two adjacent crop sites found essentially in the same 0.05° model grid. The simulated NEE may agree better with the average observed NEE of two crop sites. Hourly measured NEE at crop sites range from –64.4 to +28.1 μmol m^{-2} s^{-1} while simulated values span from –66.7 to +12.1 μmol m^{-2} s^{-1} with mean bias of –0.59 μmol m^{-2} s^{-1} and RMSE of 5.98 μmol m^{-2} s^{-1} over the entire observed window (**Fig. 10c**). Uncertainties/bias in the modeled hourly NEE based on these two crop sites outside Indianapolis are in proximity to those based on 11 FLUXNET crop sites (**Fig. 10b** vs. **Fig. 9**). Lastly, we focus on flux comparisons within Indianapolis. NEE fluxes at sites #1 and #4 exhibit a seasonally attenuated pattern but stronger biospheric activities in Nov and Dec compared to the crop sites (**Fig. 10c**). The correlation coefficient of hourly NEE fluxes between model and observations is 0.75. Modeled mean diurnal cycles over JJA 2018 coincide with those from observations at urban vegetation sites (**Fig. 10d**). Spatial distribution of summertime average NEE from SMUrF can be found in **Supplementary Fig. S12**.

3.2.2 SMUrF vs. UrbanVPRM for Los Angeles

The comparisons of SMUrF to dozens of EC sites have yet to offer much insight into the spatial distribution of urban CO_2 fluxes. Therefore, we further compare SMUrF against urbanVPRM simulation (**Sect. 2.1.5**) at 30-m grid spacing over Los Angeles from July to Sept 2017. SMUrF and urbanVPRM agree with respect to the spatial distribution of estimated GEE fluxes, e.g., stronger uptakes over mountainous and residential areas to the northeast of Pasadena and San Bernardino and nearly zero uptake over the Moreno Valley to the south of Riverside and the LA basin (**Fig. 11a**). SMUrF simulates a stronger biospheric uptake than urbanVPRM across LA over JAS in 2017 (1st column in **Fig. 11a**).

Both models incorporated observed GPP from EC sites for tuning their parameters but are driven with different spatial proxies (SIF vs. EVI and LSWI) with different model formulations. As one of the key improvements, urbanVPRM revises the initial VPRM-based R$_{eco}$ by incorporating impervious surface areas (ISA), which in turns modify the air temperature over urban cores due to urban heat island (T$_{UHI}$) effect and affect estimated GPP, autotrophic and heterotrophic respirations. For example, R$_H$ can be reduced while R$_A$ and GPP may be increased given enhanced T$_{UHI}$ over higher ISA regions in urbanVPRM. Regardless, T$_{UHI}$-revised R$_{eco}$ in urbanVPRM still follows a simple function of air temperature. ISA is implicitly contained in SIF although

not explicitly considered in SMUrF. R_{eco} in SMUrF is driven not only by air temperatures but also soil temperatures and GPP. Thus, R_{eco} in SMUrF appears to be more correlated spatially with its GPP. An overall higher R_{eco} and more positive NEE is associated with SMUrF compared to urbanVPRM over LA (3rd column in **Fig. 11a**), attributed to methodological discrepancies in producing R_{eco}. Similarly, the 3-month mean diurnal cycles of hourly NEE extracted from a few grids indicate stronger daily

5   amplitudes according to SMUrF (**Fig. 11b**). Both models suggest Pasadena, towards the northern end of LA basin, is associated with a slightly stronger diurnal amplitude than downtown LA, with discrepancies in the hourly NEE during noon hours likely because of differences in the data products from which PAR or SW_{rad} are derived (e.g., cloud coverage and spatial resolution).

Despite the opposing signs between urbanVPRM and SMUrF modeled NEE over the LA basin, the overall biological

10   activity (either net positive or negative) remains small, particularly when $FFCO_2$ emissions are compared. As a quick analysis, we defined "downtown LA" as a rectangle with the following lat/long boundaries: 118.5°W–118°W and 33.9°N – 34.1°N and removed one gridcell with intensive $FFCO_2$ emissions from consideration (likely due to point sources, **Fig. 11c**). The average $FFCO_2$ over JAS 2017 within downtown LA is ~12.1 μmol m^{-2} s^{-1}, while differences in NEE between two biogenic models remain small, at ~0.41 μmol m^{-2} s^{-1}.

15   ### 3.3 Urban-rural gradient in $XCO_{2.ff}$ and $XCO_{2.bio}$

After presenting the hourly NEE evaluations and urban-rural contrast around 40 cities, we examined the imprint of urban-rural NEE contrasts on CO_2 concentrations. As described in **Sect. 2.6**, we analyzed OCO-2 XCO_2 observations over a few cities and accounted for the atmospheric transport between upwind carbon sources/sinks and downwind satellite soundings as reflected by X-STILT's column footprints (**Fig. 12a**). Only places with non-zero footprints and non-zero fluxes contribute to downwind

20   XCO_2 anomalies, which can be visualized by the spatial contribution of $XCO_{2.ff}$ enhancements and $XCO_{2.bio}$ anomalies in **Fig. 12cd**. The sum of those spatially-explicit XCO_2 contributions serves as the total anthropogenic or biogenic XCO_2 anomalies per receptor (**Fig. 12b**).

Boston provides the main case study here as its anthropogenic and biogenic fluxes have been extensively studied by previous

25   studies (Decina et al., 2016; Hardiman et al., 2017; Sargent et al., 2018), notwithstanding the small number of qualified OCO-2 tracks. On July 7, 2018, the northeasterly wind transported air from Boston to downwind satellite soundings with an overpass time of ~1700 UTC or 1300 LT (**Fig. 12a**). Over the near-field area immediately around satellite soundings, most biogenic contributions stayed negative due to daytime photosynthetic uptake (green colors in **Fig. 12d**) where strong surface influences are found (**Fig. 12a**). During the few hours prior to 1300 LT, air parcels within the planetary boundary layer began to encounter

30   net biogenic release away from the receptors, leading to slightly positive biogenic contributions in XCO_2 (light-yellow colors in **Fig. 12d**). Yet, strong negative near-field anomalies prevail over the slightly positive far-field anomalies, resulting in total negative $XCO_{2.bio}$ at the receptors spanning from –2 to –0.3 ppm (green dots in **Fig. 12b**). The convolution between footprints

and FFCO$_2$ emissions is simpler, always yielding positive enhancements (**Fig. 12c**), especially over soundings from 41.7 ° to 42.3° N with XCO$_{2.ff}$ enhancements of up to 0.6 ppm (orange dots in **Fig. 12b**).

We then take a closer look at the modeled XCO$_2$ anomalies along latitude (**Fig. 12b**). XCO$_2$ anomalies to the south of the urban peak are close to zero due to minimal influences from either FFCO$_2$ or NEE. Moving northward, soundings started to experience intensive biogenic activities that lead to XCO$_{2.bio}$ anomalies of up to –2 ppm. Due to a less active urban biosphere than its surrounding vegetation, a rise in XCO$_{2.bio}$ has been spotted centered at ~41.9° N relative to the adjacent latitude bands centered at ~41.7 or 42.2° N. That being said, the urban-rural gradient in XCO$_{2.bio}$ anomalies (hereinafter "ΔXCO$_{2.bio}$") can exceed 0.5 ppm, which is comparable to the maximum XCO$_{2.ff}$ of 0.6 ppm. We will discuss the implication of this urban-rural bio-gradient ΔXCO$_{2.bio}$ in the context of the total measured XCO$_2$ in **Sect. 4.1** (**Fig. 12e**).

Clearly, ΔXCO$_{2.bio}$ can vary with locations and time of day or year when measurements were taken. We studied a few more OCO-2 tracks near Indianapolis, Salt Lake City, and Rome given their different surrounding vegetation types (**Fig. 13**). These summertime tracks were picked given their richness in screened soundings (quality flag = 0) that facilitates the X-STILT modeling. Although the OCO-2 track is adjacent to Indianapolis at 1800UTC on July 13, 2018, upwind regions are located to the east of the soundings and away Indianapolis leading to minimal XCO$_{2.ff}$ anomalies and strong biospheric uptake with XCO$_{2.bio}$ below –2 ppm (**Fig. 13ab**). Strong influence with the surface land is concentrated within the Salt Lake Valley on June 25, 2018, leading to a maximum XCO$_{2.ff}$ of 0.5 ppm and XCO$_{2.bio}$ with comparable magnitude but negative signs (**Fig. 13ef**). For Rome, strong footprints to the southwest of the city center interact with positive NEE, giving rise to XCO$_{2.bio}$ anomalies of up to 1.5 ppm over 42°– 42.5°N where XCO$_{2.ff}$ are equally significant (**Fig. 13j**). To sum up, XCO$_{2.bio}$ anomalies can be associated with either sign and an absolute magnitude of up to 2.5 ppm during growing seasons, as seen in cases of Indianapolis and Boston. The urban-rural bio-gradient ΔXCO$_{2.bio}$ is smaller, with maximum values ranging from 0.6 to 1.0 ppm among our limited cases (2nd column in **Fig. 13**). Based on the limited cases, XCO$_{2.bio}$ anomalies are normally less negative (more positive) within the urban-enhanced region, serving as a peak that coincides with the XCO$_{2.ff}$ peak. More cities and satellite tracks, accompanied by comprehensive error analyses should be examined in the future to verify these statements.

4 Discussion and summary

We now discuss some applications and limitations of SMUrF, and in particular, examine how an urban-rural gradient in XCO$_{2.bio}$ may alter the interpretation of XCO$_2$ observations during the growing seasons.

4.1 Implications on background XCO$_2$ determination

As the extraction of urban emissions from column measurements can be sensitive to the background definition (e.g., Wu et al., 2018), we illustrate the impact of urban-rural gradient in XCO$_{2.bio}$ during the growing season in the context of

background determinations. Let us consider the background XCO_2 ($XCO_{2.bg}$) defined as the average of observations over region unaffected by urban emissions. Observed enhancements are then calculated as levels of XCO_2 elevated above $XCO_{2.bg}$. This constant $XCO_{2.bg}$ reasonably represents the XCO_2 portion unaffected by urban emissions during non-growing seasons for most places (Wu et al., 2018). However, this background definition might implicitly neglect the variation in biospheric XCO_2 anomalies between the urban-enhanced versus the background region. Again, it is the gradient in $XCO_{2.bio}$, not its absolute level, along satellite tracks that modify the background value.

The goal, then, becomes to create a latitude-dependent background—$XCO_{2.bg}$ (lat) in **Eq. 3**—that integrates the adjustment of urban-rural biospheric gradient ($\Delta XCO_{2.bio}$). To quantify the $\Delta XCO_{2.bio}$ correction term, we average $XCO_{2.bio}$ within the background latitude band ($XCO_{2.bio.bg}$) and subtract it from the latitude-varying $XCO_{2.bio}$. The correction term is then added to the constant background ($XCO_{2.bg.const}$) to yield a latitudinally varying, bio-adjusted background:

$$XCO_{2.bg} \text{ (lat)} = XCO_{2.bg.const} + \Delta XCO_{2.bio} \text{ (lat)}$$
$$= XCO_{2.bg.const} + XCO_{2.bio} \text{ (lat)} - XCO_{2.bio.bg}. \tag{3}$$

Recall that $XCO_{2.bio}$ (lat) is the modeled biospheric anomalies using SMUrF and X-STILT (**Sects. 2.6** and **3.3**).

To facilitate visualization and understanding of $\Delta XCO_{2.bio}$ and bio-adjusted background, let us return to the Boston case (**Fig. 12**). Following the "overpass-specific approach" proposed in Wu et al. (2018), we estimated the urban plume (black curve in **Supplementary Fig. S13a**) and defined the background latitude range of 42.26°– 42.76° N (light green ribbon in **Fig. 12e**). The constant background is 403.37 ppm (dark green line in **Fig. 12e**) with an uncertainty of 1.03 ppm containing both retrieval errors and observational noise (**Supplementary Fig. S13b**). The mean $XCO_{2.ff}$ and $XCO_{2.bio}$ anomalies within the background region are 0.23 ppm and –1.41 ppm, respectively. After integrating the bio-gradient $\Delta XCO_{2.bio}$, a new bio-adjusted background varies along latitude (light green line in **Fig. 12e**). If modeled $XCO_{2.ff}$ is added to the bio-adjusted background, the resultant total XCO_2 better reproduces the latitudinal variations of the measured mean values (**Fig. 12e**). Both the observed XCO_2 and modeled XCO_2 with the $\Delta XCO_{2.bio}$ correction term exhibit dips in XCO_2 on both sides outside the urban peak, which is missing from the model result using the constant background (orange line in **Fig. 12e**).

A more comprehensive error analysis of various modeled and observed errors is needed to draw further quantitative conclusions from the model-data XCO_2 comparison. For instance, modeled XCO_2 appears to extend wider latitudinally with a lower amplitude and a small latitude shift of ~0.1° compared to observed XCO_2 (purple line versus black triangles in **Fig 12e**) likely due to bias in wind speed and direction. Nonetheless, neglecting the latitudinal/spatial gradient in biogenic XCO_2 anomalies given gradients in NEE can affect the extracted urban signal and inferred $FFCO_2$ emissions.

4.2 Limitation and future improvement

This study aims at offering a model representation of biogenic CO_2 fluxes to help improve the CO_2 flux partitioning over cities worldwide. SMUrF takes advantage of SIF to estimate GPP from urban to rural areas and incorporates multiple predictors to estimate R_{eco} using neural network approach. Here we identify several model limitations and room for future improvements.

The adoption of SIF has dramatically benefited the GPP calculation over urban areas around the globe, as non-vegetated surfaces within the satellite footprint do not contribute to observed signals. However, the main caveat lies in the assumption of linear GPP-SIF relationship and one set of constant α values across all seasons used in SMUrFv1. Previous research (Magney et al., 2020; Miao et al., 2018; Wohlfahrt et al., 2018; Yang et al., 2018) revealed divergence of the empirical linear

10 GPP-SIF relation at sub-diurnal and leaf scales, and under certain environmental conditions (low light, or high light & stress), owing to competing fluorescence, photochemical, and non-photochemical pathways for the absorbed light (Magney et al., 2020). For example, Yang et al. (2018) suggest considering additional environmental and biophysical factors related to the modeling of light use efficiency, e.g., relative humidity, cloudiness, and growth stage of crops, to improve SIF-based GPP estimates. Although multiple studies have shown dependence of the linear slope on PFT (e.g., Guanter et al., 2012; Sun et al.,

15 2017; Turner et al., 2021), further research is needed to understand the scale dependence of the GPP-SIF relation, and determine if an inflection point for linearity exists. Given noise/uncertainty in the CSIF product and EC tower data across multiple continents, we apply a simple linear regression fit and let the uncertainty analysis incorporate deviations from the linear assumption. Future iterations of SMUrF can test alternative statistical fits with physical fundamentals or expand the GPP-SIF slopes across seasons, and new urban land cover maps (e.g., Coleman et al., 2020).

Mixed pixels are difficult to account for in heterogenous urban environments if without much information on the local biosphere. As a general solution that can be widely applied to cities around the world, we derived and utilized the relationship between relative tree fractions and AGB. This relationship is a simplification proposed from high-resolution land cover data over Los Angeles. Fortunately, recent work using high resolution airborne and satellite imagery demonstrates that urban land

25 cover mapping capabilities are improving (e.g., Coleman et al., 2020). Other advanced space sensors provide SIF retrieval with a broader coverage over cities, land surface temperatures, biomass, and canopy structures of forests at an unprecedented spatiotemporal resolution (Stavros et al., 2017). Examples of such satellite sensors include OCO-3 (Eldering et al., 2019), the ECOsystem Spaceborne Thermal Radiometer Experiment ECOSTRESS (Fisher et al., 2020) and the Global Ecosystem Dynamics Investigation LIDAR (GEDI, Duncanson et al., 2020), all onboard the International Space Station. These cutting-

30 edge and future data streams may improve the approximation of tree types and fraction over cities and flux estimates in SMUrF.

SMUrF parameters can be fined tuned for more localized applications, such as using higher resolution shortwave radiation or PAR data with higher accuracy in cloud cover estimates. Further, the reference temperature used in this work (30° C) can be a

bit higher than that (20° C) used in the calculation of maintenance respiration and (25°C) in the calculation of heterotrophic respiration in CLM. The Q_{10} parameter (here = 1.5) also varies significantly in space and time. Moreover, a few secondary-order ecological and environmental variables may affect biogenic fluxes. For example, we have tried adding soil moisture as an explanatory variable into the R_{eco} training system, but the improvement in model performance is not that evident.

More challenging is the shortcoming that current flux estimates in SMUrF over cities still rely on relationships derived from observations over natural biomes. Urban trees are found to possess different characteristics from natural trees (Smith et al., 2019), which pose a difficult task for biospheric models without more dedicated observations and mechanistic understanding of the urban environment. Anthropogenic moisture input (i.e., urban irrigation) has been found to effectively influence urban

10 biogenic fluxes, particularly over (semi)arid residential areas (Johnson and Belitz, 2012; Vahmani and Hogue, 2014; Miller et al., 2021). Although we currently rely on SIF to pick up possible irrigation effect on GPP, it would be interesting to explore the linkage between water and carbon fluxes in future analyses.

Because atmospheric CO_2 concentrations measured from satellites are mainly influenced by the anthropogenic and biogenic

15 carbon fluxes a few hours to days ahead of the overpass time, this work focused on presenting and evaluating the diurnal and seasonal CO_2 fluxes. Biogenic CO_2 fluxes at other moments, e.g., their interannual variations and trend, may require further investigations. We hope to examine more cities and different times of the day in future studies to better quantify the relative biogenic and anthropogenic contributions to XCO_2 anomalies. Incorporating uncertainties in biogenic fluxes and resultant $XCO_{2.bio}$ is needed for future top-down studies with aims of quantifying urban signals especially over growing seasons.

Lastly, we summarize the potential applications of SMUrF as follows.
1) *Improve the separation between biogenic and anthropogenic CO_2 fluxes for urban studies*. Regardless of the exact approach adopted for background definition, researchers can combine atmospheric transport models with fluxes from SMUrF to get estimates of the CO_2 anomalies due to biogenic flux exchanges, as shown in **Sect. 4.1**.

25 2) *Fill-in the urban gap and assist regional flux inversions*. The state-of-art terrestrial models that go into flux inversions usually include global models with relatively coarse resolution (e.g., 4° by 5°) with possible downscaling approaches. At the other end of the spectrum are highly localized models at fine resolution but sometimes requiring customization for individual cities. SIF-based fluxes from SMUrF may help bridge between the continental scale and the urban scale, with reasonable fine resolution and regional to global coverage.

30 3) *Understand how urbanization modifies the planet and environment.* SMUrF offers a quick solution to the biogenic fluxes within urban areas and their rural surroundings, which provide insights on how biogenic CO_2 fluxes vary among cities with different urban planning and emissions.

Data and code availability

The source codes of SMUrF with the latest changes are stored at the GitHub repository on https://github.com/wde0924/SMUrF. The exact version of the SMUrF model used in this work is archived on Zenodo (Wu et al., 2020b). SMUrF modeled output can be accessed from the Oak Ridge National Lab DAAC, including the 1) 4-day mean CSIF-based GPP and uncertainty, 2) daily mean NN-based R_{eco}, and 3) the final hourly GPP, R_{eco}, and NEE fluxes. Because running the model for the entire globe incurs significant computational cost, we only shared the flux results for the following eight regions: western CONUS [125 W – 95 W, 25 N – 50 N]; eastern CONUS [95 W – 65 W, 25 N – 50 N]; western Europe [11W – 20 E, 35 N – 60 N]; eastern China [100 E – 125E, 20 N – 50 N]; eastern Asia [125 E – 150 E, 30 N – 55 N]; eastern Australia [130 E – 155 E, 40 S – 10 S], south America [65 W – 40 W, 40 S – 10 S], and central Africa [10 W – 20 E, 10 S – 15 N].

Instructions for running SMUrF: The user should start with main scripts of *main_script_*.r* in sequence for computing gridded GPP, R_{eco}, and NEE, since the calculation of R_{eco} using *main_script_Reco.r* relies on GPP generated using *main_script_GPP.r*. Model-related subroutines written in R/3.6.1 are stored in SMUrF/r/src with model-required dependences in SMUrF/data. For most of the cases, the user does not need to modify these subroutines. Model developments are ongoing and please contact the corresponding author if one would like to obtain model outputs for other regions/cities.

Required input data products for driving SMUrF (data citation; parameter name in the model script).
1) Clear-sky SIF provided by CSIF (Zhang et al., 2018; *csif.cpath*)
2) AGB from GlobBiomass (Santoro et al. 2018; *agb.path*)
3) MCD12Q1 v006 (Friedl and Sulla-Menashe, 2019; *lc.path*), accessed from the **App**lication for **E**xtracting and **E**xploring **A**nalysis **R**eady **S**amples (AρρEEARS). See README.md on GitHub repository for info on how to download the exact format that SMUrF requires
4) Hourly air temperature and shortwave radiation downwards from ERA5 reanalysis (Copernicus Climate Change Service Information, 2017; *TA** and *SSRD**)

Other important data products used in this paper (not prerequisites for driving SMUrF) include:
1) high-resolution 60 cm NAIP-based urban land cover classification product (Coleman, 2020) from Mendeley Data,
2) ODIAC emission data product available from the Global Environmental Database hosted by the Center for Global Environmental Research at the National Institute for Environmental Studies (Oda and Maksyutov, 2015),
3) EC measurements from FLUXNET2015 (Pastorello et al., 2017).

Appendix A. Comparison of CSIF with TROPOMI-based downscaled SIF and vegetation fraction from WUDAPT

We carried out two tests to verify the accuracy and capability of CSIF. Firstly, CSIF is compared against a newly developed SIF product from TROPOMI over the Contiguous United States (CONUS) from June to August in 2018 (Turner et al. 2020, 2021). This downscaled TROPOMI-based SIF product is initially available at 500 m and then averaged to 0.05° for the comparison. Due to the discrepancies in the reported SIF retrieval wavebands between OCO-2 (757 and 771 nm) and TROPOMI (740 nm), the OCO-2 based CSIF (757 nm) is scaled by an empirical scaling factor of 1.56 (Köhler et al., 2018) to yield comparison with TROPOMI SIF at the far-red SIF peak of 740 nm. Note that this scaling factor of 1.56 is only applied here for model comparisons and not for flux calculations. OCO-2 based CSIF and TROPOMI-based SIF both see high biological activities over the eastern CONUS and agree well spatially (**Supplementary Fig. S2**). Model-model mismatch can be attributed to their different approaches and adopted observations. For example, CSIF uses broadband reflectances as indicators whereas downscaled TROPOMI SIF product benefits from TROPOMI's wider and denser spatial coverage. Nevertheless, CSIF-based α values (mostly > 20 (μmol m^{-2} s^{-1}) (mWm^{-2} sr^{-1} nm^{-1})$^{-1}$) are higher than TROPOMI-based α ranging from 13.5 to 18 (μmol m^{-2} s^{-1}) (mWm^{-2} sr^{-1} nm^{-1})$^{-1}$ reported in Turner et al. (2020) and Turner et al. (2021), which potentially compensate for the SIF mismatch.

We also relate CSIF to vegetated and impervious fractions with a spatial resolution of 10 km from the World Urban Database and Access Portal Tools (WUDAPT) project (Ching et al., 2018) for a few available US cities. WUDAPT is "an international community-generated urban canopy information and modeling infrastructure to facilitate urban-focused climate, weather, air quality, and energy-use modeling application studies" (Ching et al., 2018). The Local Climate Zones (LCZ) provided by WUDAPT contain 10 specific classifications for the urban areas and 7 natural types with characterizations of surface property/structure (e.g., building and tree height and density) and surface cover (pervious vs. impervious) (Stewart and Oke, 2012). Each LCZ classification is associated with a range of fractions for impervious land, building, and vegetation, such as 40 – 60 % of impervious percentage for compact high rise (Ching et al., 2018). We calculated the mean impervious and vegetated fractions for every LCZ and projected those fractions to CSIF's grids. Consequently, spatial gradient of CSIF coincides with that of vegetated fractions estimated from WUDAPT, as suggested by the increasing trend moving away from urban cores (**Supplementary Fig. S3**). Thus, CSIF nicely reveals the urban-rural contrast in biological activities.

Since CSIF nicely mimic the urban-rural gradient, additional information about vegetated/impervious fractions was not necessary in the calculation of α for every 500 m urban grid. For instance, if half of the 0.05° urban grid cell is covered by impervious land with the rest half covered by DBFs, SIF of this grid cell would already be lower than SIF of a grid cell fully covered by DBFs. Thus, instead of calculating a weighted mean α using slopes and land fractions of DBF and impervious land (whose $\alpha = 0$), we only need to assign the α of DBF to this particular 500 m urban grid. Otherwise, the resultant urban GPP (= CSIF * α) could be underestimated by "double-counting" of impervious fraction in both SIF and α.

Appendix B. Technical note on R$_{eco}$ prediction

As introduced in **Sect. 2.3**, we have tested three ways to predict R$_{eco}$ by applying

M1)   one NN model trained using data points with all biomes to 0.05° grids, except for water, ice, and barren land, without considering sub-gridcell variations in land cover types,

5   M2)   one NN model with biome and month and season of the year as additional categorical variables (with one-hot encoding),

M3)   multiple biome-specific NN models to 500 m grids with different biomes and aggregating predicted R$_{eco}$ to 0.05°.

Technically speaking, we tried both the built-in R package Neuralnet (Fritsch et al., 2016) as well as the R interface for Keras (Falbel et al., 2019) that is a high-level neural networks API based on backend including TensorFlow to build NN models.

10   Although M1 benefits from larger amount of sample data and shorter processing time in predicting R$_{eco}$ without matching NN models with land cover types at 500 m, M2 approach is physically more meaningful as the temperature dependence of respiration may vary among different vegetation species. In particular, being able to resolve sub-gridcell variations and different vegetation fractions (processed during GPP estimates, **Sect. 2.2.2**) facilitates a more reasonable R$_{eco}$ calculation over urban areas. Note that modeled T$_{air}$ and T$_{soil}$ have been bilinearly interpolated from their initial grid spacings onto the required

15   grid spacing. In the ends, we used the last M3 approach given its better performance.

Before training neural network models, we removed a few flux sites with relatively large RMSE values between modeled versus observed GPP to avoid erroneous information being transformed into the training process of R$_{eco}$ (**Supplementary Fig. S14**). All explanatory and response variables have been linearly normalized to values between [0, 1] based on their maximum

20   and minimum values before training. Adjusting the raw data to a common scale may dramatically speed up the training process and avoid the situation where the predicting variable appears to be more sensitive to one of the response variables. To determine the hyper-parameters that work the best on our data and help avoid under-/over-fitting situation, we carried out a 5-fold cross-validation (**Supplementary Fig. S15**). That being said, 80 % of the data serves as the training set with the remaining 20 % as the validation set. The 5-fold cross validation can be viewed as repeated holdouts and the average errors will be calculated

25   after five different holdouts. The main hyper-parameter tested here is the number of neurons (8, 16, 32, or 64 neurons per layer) for a two-layer model. The overall RMSE and loss function between predicted and observed R$_{eco}$ on the validating set turn out to be similar among different numbers of neurons. In addition, loss functions on the training and validating sets appear to be similar, implying no strong sign of overfitting.

Author contributions. DW and JCL designed the study and DW is responsible for model scripts. JCL and HD offered

30   constructive insights regarding the construction and development of SMUrF. JCL, TO and EAK contributed to the design of

model result presentation. VY and NP provided the urbanVPRM model outputs for LA for flux comparison with SMUrF. All authors contributed to the editing of the final manuscript.

Competing interests. The authors declare that they have no conflict of interest.

Acknowledgement

5   This work is based upon work supported by the National Aeronautics and Space Administration funding under grants NNX15AI40G, NNX15AI41G, NNX15AI42G, 80NSSC19K0196, 80NSSC19K0093, and 80NSSC20K0010. TO is supported by NASA grants NNX14AM76G, 80NSSC18K1307, and 80NSSC18K1313. The resources and support from the Center for High-Performance Computing at the University of Utah are gratefully acknowledged. VY and NCP acknowledge funding by the NASA OCO-2 Science Team, grant number 17-OCO2-17-0025. A portion of this research was carried out at the Jet

10 Propulsion Laboratory, California Institute of Technology, under a contract with the National Aeronautics and Space Administration. We are grateful to Ken Davis and Kai Wu at the Penn State University for sharing INFLUX data and providing constructive comments on this manuscript. We acknowledge Alex Turner at the Univ. of Washington for sharing the downscaled TROPOMI SIF data over the entire CONUS from June to Aug 2018. We thank Yao Zhang at the Lawrence Berkeley National Laboratory for sharing the 0.05° CSIF fields and for helpful discussions. DW also appreciates assistance

15 from Guannan Wei (Purdue Univ.) and Benjamin Fasoli (Univ. of Utah) on the construction and evaluation of Neural Network models and discussions with Liyin He (Caltech) on the C3/C4 partitioning. Lastly, we appreciate all the constructive feedbacks from the two reviewers.

References

20   Chen, J., Zhao, F., Zeng, N. and Oda, T.: Comparing a global high - resolution downscaled fossil fuel - CO2 emission dataset to local inventory - based estimates over 14 global cities, Carbon Balance Manag., 1–15, doi:10.1186/s13021-020-00146-3, 2020.

Ching, J., Mills, G., Bechtel, B., See, L., Feddema, J., Wang, X., Ren, C., Brorousse, O., Martilli, A., Neophytou, M., Mouzourides, P., Stewart, I., Hanna, A., Ng, E., Foley, M., Alexander, P., Aliaga, D., Niyogi, D., Shreevastava, A.,
25   Bhalachandran, P., Masson, V., Hidalgo, J., Fung, J., Andrade, M., Baklanov, A., Dai, W., Milcinski, G., Demuzere, M., Brunsell, N., Pesaresi, M., Miao, S., Mu, Q., Chen, F. and Theeuwesits, N.: WUDAPT: An urban weather, climate, and environmental modeling infrastructure for the anthropocene, Bull. Am. Meteorol. Soc., 99(9), 1907–1924, doi:10.1175/BAMS-D-16-0236.1, 2018.

Coleman, R. W., Stavros, E. N., Yadav, V. and Parazoo, N.: A Simplified Framework for High-Resolution Urban Vegetation
30   Classification with Optical Imagery in the Los Angeles Megacity, Remote Sens., 12(15), 2020.

Coleman, Red Willow: Southern California 60-cm Urban Land Cover Classification, Mendeley Data, V1, doi: 10.17632/zykyrtg36g.1, 2020.

Copernicus Climate Change Service (C3S): ERA5: Fifth generation of ECMWF atmospheric reanalyses of the global climate. Copernicus Climate Change Service Climate Data Store (CDS). https://cds.climate.copernicus.eu/cdsapp#!/home, doi:
35   10.24381/cds.bd0915c6, 2017. Accessed 2020-04-14.

Crisp, D., Fisher, B. M., O'Dell, C., Frankenberg, C., Basilio, R., Bösch, H., Brown, L. R., Castano, R., Connor, B., Deutscher, N. M., Eldering, A., Griffith, D., Gunson, M., Kuze, A., Mandrake, L., McDuffie, J., Messerschmidt, J., Miller, C. E., Morino, I., Natraj, V., Notholt, J., O'Brien, D. M., Oyafuso, F., Polonsky, I., Robinson, J., Salawitch, R., Sherlock, V., Smyth, M., Suto, H., Taylor, T. E., Thompson, D. R., Wennberg, P. O., Wunch, D. and Yung, Y. L.: The ACOS CO2 retrieval algorithm
40   – Part II: Global XCO2 data characterization, Atmos. Meas. Tech., 5(4), 687–707, doi:10.5194/amt-5-687-2012, 2012.

Decina, S. M., Hutyra, L. R., Gately, C. K., Getson, J. M., Reinmann, A. B., Short Gianotti, A. G. and Templer, P. H.: Soil respiration contributes substantially to urban carbon fluxes in the greater Boston area, Environ. Pollut., 212, 433–439, doi:10.1016/j.envpol.2016.01.012, 2016.

Dietze, M. C., Vargas, R., Richardson, A. D., Stoy, P. C., Barr, A. G., Anderson, R. S., Arain, M. A., Baker, I. T., Black, T.
45   A., Chen, J. M., Ciais, P., Flanagan, L. B., Gough, C. M., Grant, R. F., Hollinger, D., Izaurralde, R. C., Kucharik, C. J., Lafleur, P., Liu, S., Lokupitiya, E., Luo, Y., Munger, J. W., Peng, C., Poulter, B., Price, D. T., Ricciuto, D. M., Riley, W. J., Sahoo, A. K., Schaefer, K., Suyker, A. E., Tian, H., Tonitto, C., Verbeeck, H., Verma, S. B., Wang, W. and Weng, E.: Characterizing the performance of ecosystem models across time scales: A spectral analysis of the North American Carbon Program site-level synthesis, J. Geophys. Res. Biogeosciences, 116(4), doi:10.1029/2011JG001661, 2011.

50   Duncanson, L., Neuenschwander, A., Hancock, S., Thomas, N., Fatoyinbo, T., Simard, M., Silva, C. A., Armston, J., Luthcke, S. B., Hofton, M., Kellner, J. R. and Dubayah, R.: Biomass estimation from simulated GEDI, ICESat-2 and NISAR across environmental gradients in Sonoma County, California, Remote Sens. Environ., 242(April), 111779, doi:10.1016/j.rse.2020.111779, 2020.

Duveiller, G. and Cescatti, A.: Spatially downscaling sun-induced chlorophyll fluorescence leads to an improved temporal
55   correlation with gross primary productivity, Remote Sens. Environ., 182, 72–89, doi:10.1016/j.rse.2016.04.027, 2016.

Duveiller, G., Filipponi, F., Walther, S., Köhler, P., Frankenberg, C., Guanter, L. and Cescatti, A.: A spatially downscaled sun-induced fluorescence global product for enhanced monitoring of vegetation productivity, Earth Syst. Sci. Data, 12(2), 1101–1116, doi:10.5194/essd-12-1101-2020, 2020.

Eldering, A., Taylor, T. E., O'Dell, C. W. and Pavlick, R.: The OCO-3 mission: measurement objectives and expected performance based on 1 year of simulated data, Atmos. Meas. Tech., 12(4), 2341–2370, 2019.

Ellis, E. C. and Ramankutty, N.: Putting people in the map: Anthropogenic biomes of the world, Front. Ecol. Environ., 6(8), 439–447, doi:10.1890/070062, 2008.

Falbel, D., Allaire, J. J., and Chollet, F.: keras: R Interface to 'Keras' version 2.2.5.0, https://keras.rstudio.com/index.html, 2019. Accessed 2020-04-14.

Fasoli, B., Lin, J. C., Bowling, D. R., Mitchell, L. and Mendoza, D.: Simulating atmospheric tracer concentrations for spatially distributed receptors: updates to the Stochastic Time-Inverted Lagrangian Transport model's R interface (STILT-R version 2), Geosci. Model Dev., 11(7), 2813–2824, 2018.

Fisher, J. B., Sikka, M., Huntzinger, D. N., Schwalm, C. and Liu, J.: 3-hourly temporal downscaling of monthly global terrestrial biosphere model net ecosystem exchange, Biogeosciences, 13(14), 2016.

Fisher, J. B., Lee, B., Purdy, A. J., Halverson, G. H., Dohlen, M. B., Cawse-Nicholson, K., Wang, A., Anderson, R. G., Aragon, B., Arain, M. A., Baldocchi, D. D., Baker, J. M., Barral, H., Bernacchi, C. J., Bernhofer, C., Biraud, S. C., Bohrer, G., Brunsell, N., Cappelaere, B., Castro-Contreras, S., Chun, J., Conrad, B. J., Cremonese, E., Demarty, J., Desai, A. R., De Ligne, A., Foltýnová, L., Goulden, M. L., Griffis, T. J., Grünwald, T., Johnson, M. S., Kang, M., Kelbe, D., Kowalska, N., Lim, J. H., Maïnassara, I., McCabe, M. F., Missik, J. E. C., Mohanty, B. P., Moore, C. E., Morillas, L., Morrison, R., Munger, J. W., Posse, G., Richardson, A. D., Russell, E. S., Ryu, Y., Sanchez-Azofeifa, A., Schmidt, M., Schwartz, E., Sharp, I., Šigut, L., Tang, Y., Hulley, G., Anderson, M., Hain, C., French, A., Wood, E. and Hook, S.: ECOSTRESS: NASA's Next Generation Mission to Measure Evapotranspiration From the International Space Station, Water Resour. Res., 56(4), 1–20, doi:10.1029/2019WR026058, 2020.

Frankenberg, C., Butz, A. and Toon, G. C.: Disentangling chlorophyll fluorescence from atmospheric scattering effects in O_2 A-band spectra of reflected sun-light, Geophys. Res. Lett., 38(3), 1–5, doi:10.1029/2010GL045896, 2011.

Friedl, M., and Sulla-Menashe. D.: MCD12Q1 MODIS/Terra+Aqua Land Cover Type Yearly L3 Global 500m SIN Grid V006, distributed by NASA EOSDIS Land Processes DAAC, doi:10.5067/MODIS/MCD12Q1.006, 2019 Accessed 2020-04-14.

Fritsch, S., Guenther, F., and Guenther, M. F: Package 'neuralnet' version 1.44.2. The Comprehensive R Archive Network, 2016. https://github.com/bips-hb/neuralnet, Accessed 2020-04-14.

George, K., Ziska, L. H., Bunce, J. A. and Quebedeaux, B.: Elevated atmospheric CO_2 concentration and temperature across an urban-rural transect, Atmos. Environ., 41(35), 7654–7665, doi:10.1016/j.atmosenv.2007.08.018, 2007.

Guanter, L., Zhang, Y., Jung, M., Joiner, J., Voigt, M., Berry, J. A., Frankenberg, C., Huete, A. R., Zarco-Tejada, P., Lee, J.-E., Moran, M. S., Ponce-Campos, G., Beer, C., Camps-Valls, G., Buchmann, N., Gianelle, D., Klumpp, K., Cescatti, A., Baker, J. M. and Griffis, T. J.: Global and time-resolved monitoring of crop photosynthesis with chlorophyll fluorescence, Proc. Natl. Acad. Sci., 111(14), E1327–E1333, doi:10.1073/pnas.1320008111, 2014.

Hao, D., Asrar, G. R., Zeng, Y., Zhu, Q., Wen, J., Xiao, Q., and Chen, M.: DSCOVR/EPIC-derived global hourly and daily downward shortwave and photosynthetically active radiation data at 0.1° × 0.1° resolution, Earth Syst. Sci. Data, 12, 2209–2221, https://doi.org/10.5194/essd-12-2209-2020, 2020a.

95   Hao, D., Chen, M., Asrar, G. R., Zeng, Y., Zhu, Q., Wen, J., and Xiao, Q: A global DSCOVR/EPIC-based hourly/daily shortwave radiation/PAR dataset, DataHub for Pacific Northwest National Laboratory, https://doi.org/10.25584/1595069, 2020b.

Hardiman, B. S., Wang, J. A., Hutyra, L. R., Gately, C. K., Getson, J. M. and Friedl, M. A.: Accounting for urban biogenic fluxes in regional carbon budgets, Sci. Total Environ., 592, 366–372, 2017.

100 He, L., Magney, T., Dutta, D., Yin, Y., Köhler, P., Grossmann, K., Stutz, J., Dold, C., Hatfield, J., Guan, K., Peng, B. and Frankenberg, C.: From the Ground to Space: Using Solar-Induced Chlorophyll Fluorescence to Estimate Crop Productivity, Geophys. Res. Lett., 47(7), 0–3, doi:10.1029/2020GL087474, 2020.

Helm, L. T., Shi, H., Lerdau, M. T. and Yang, X.: Solar-induced chlorophyll fluorescence and short-term photosynthetic response to drought, Ecol. Appl., 30(5), 1–12, doi:10.1002/eap.2101, 2020.

105 Hilton, T. W., Davis, K. J. and Keller, K.: Evaluating terrestrial CO_2 flux diagnoses and uncertainties from a simple land surface model and its residuals, Biogeosciences, 11(2), 217–235, doi:10.5194/bg-11-217-2014, 2014.

Huntzinger, D. N., Schwalm, C., Michalak, A. M., Schaefer, K., King, A. W., Wei, Y., Jacobson, A., Liu, S., Cook, R. B., Post, W. M., Berthier, G., Hayes, D., Huang, M., Ito, A., Lei, H., Lu, C., Mao, J., Peng, C. H., Peng, S., Poulter, B., Riccuito, D., Shi, X., Tian, H., Wang, W., Zeng, N., Zhao, F. and Zhu, Q.: The North American Carbon Program Multi-Scale Synthesis
110 and Terrestrial Model Intercomparison Project -- Part 1: Overview and experimental design, Geosci. Model Dev., 6(6), 2121–2133, doi:10.5194/gmd-6-2121-2013, 2013.

Hutyra, L. R., Duren, R., Gurney, K. R., Grimm, N., Kort, E. A., Larson, E. and Shrestha, G.: Urbanization and the carbon cycle: Current capabilities and research outlook from the natural sciences perspective, Earth's Futur., 2(10), 473–495, doi:10.1002/2014EF000255, 2014.

115 Johnson, T. D. and Belitz, K.: A remote sensing approach for estimating the location and rate of urban irrigation in semi-arid climates, J. Hydrol., 414–415, 86–98, doi:10.1016/j.jhydrol.2011.10.016, 2012.

Joiner, J., Guanter, L., Lindstrot, R., Voigt, M., Vasilkov, A. P., Middleton, E. M., Huemmrich, K. F., Yoshida, Y. and Frankenberg, C.: Global monitoring of terrestrial chlorophyll fluorescence from moderate-spectral-resolution near-infrared satellite measurements: methodology, simulations, and application to GOME-2, Atmos. Meas. Tech., 6(10), 2803–2823,
120 doi:10.5194/amt-6-2803-2013, 2013.

Kettle, A. J., Kuhn, U., Von Hobe, M., Kesselmeier, J. and Andreae, M. O.: Global budget of atmospheric carbonyl sulfide: Temporal and spatial variations of the dominant sources and sinks, J. Geophys. Res. Atmos., 107(D22), ACH--25, 2002.

Knorr, W. and Heimann, M.: Uncertainties in global terrestrial biosphere modelling, Part II: Global constraints for a process-based vegetation model, Global Biogeochem. Cycles, 15(1), 227–246, doi:10.1029/1998GB001060, 2001.

125 Köhler, P., Frankenberg, C., Magney, T. S., Guanter, L., Joiner, J. and Landgraf, J.: Global retrievals of solar-induced chlorophyll fluorescence with TROPOMI: First results and intersensor comparison to OCO-2, Geophys. Res. Lett., 45(19),

10–456, 2018.

Li, X. and Xiao, J.: A Global, 0.05-Degree Product of Solar-Induced Chlorophyll Fluorescence Derived from OCO-2, MODIS, and Reanalysis Data, Remote Sens., 11(1), 517, doi:10.3390/rs11050517, 2019a.

130   Li, X. and Xiao, J.: Mapping photosynthesis solely from solar-induced chlorophyll fluorescence: A global, fine-resolution dataset of gross primary production derived from OCO-2, Remote Sens., 11(21), doi:10.3390/rs11212563, 2019b.

Lin, J. C., Gerbig, C., Wofsy, S. C., Andrews, A. E., Daube, B. C., Davis, K. J. and Grainger, C. A.: A near-field tool for simulating the upstream influence of atmospheric observations: The Stochastic Time-Inverted Lagrangian Transport (STILT) model, J. Geophys. Res. Atmos., 108(D16), 2003.

135   Lin, J. C., Gerbig, C., Wofsy, S. C., Andrews, A. E., Daube, B. C., Grainger, C. A., Stephens, B. B., Bakwin, P. S. and Hollinger, D. Y.: Measuring fluxes of trace gases at regional scales by Lagrangian observations: Application to the CO2 Budget and Rectification Airborne (COBRA) study, J. Geophys. Res. D Atmos., 109(15), 1–23, doi:10.1029/2004JD004754, 2004.

Lin, J. C., Pejam, M. R., Chan, E., Wofsy, S. C., Gottlieb, E. W., Margolis, H. A. and McCaughey, J. H.: Attributing uncertainties in simulated biospheric carbon fluxes to different error sources, Global Biogeochem. Cycles, 25(2), 1–17,
140   doi:10.1029/2010GB003884, 2011.

Luus, K. A., Commane, R., Parazoo, N. C., Benmergui, J., Euskirchen, E. S., Frankenberg, C., Joiner, J., Lindaas, J., Miller, C. E., Oechel, W. C., Zona, D., Wofsy, S. and Lin, J. C.: Tundra photosynthesis captured by satellite-observed solar-induced chlorophyll fluorescence, Geophys. Res. Lett., 44(3), 1564–1573, doi:10.1002/2016GL070842, 2017.

MacBean, N., Maignan, F., Bacour, C., Lewis, P., Peylin, P., Guanter, L., Köhler, P., Gómez-Dans, J. and Disney, M.: Strong
145   constraint on modelled global carbon uptake using solar-induced chlorophyll fluorescence data, Sci. Rep., 8(1), 1–12, doi:10.1038/s41598-018-28697-z, 2018.

Magney, T. S., Frankenberg, C., Fisher, J. B., Sun, Y., North, G. B., Davis, T. S., Kornfeld, A. and Siebke, K.: Connecting active to passive fluorescence with photosynthesis: a method for evaluating remote sensing measurements of Chl fluorescence, New Phytol., 215(4), 1594–1608, doi:10.1111/nph.14662, 2017.

150   Magney, T. S., Bowling, D. R., Logan, B. A., Grossmann, K., Stutz, J., Blanken, P. D., Burns, S. P., Cheng, R., Garcia, M. A., Kohler, P. and others: Mechanistic evidence for tracking the seasonality of photosynthesis with solar-induced fluorescence, Proc. Natl. Acad. Sci., 116(24), 11640–11645, 2019.

Magney, T. S., Barnes, M. L. and Yang, X.: On the co-variation of chlorophyll fluorescence and photosynthesis across scales, 1–12, doi:10.1029/2020GL091098, 2020.

155   Maguire, A. J., Eitel, J. U. H., Griffin, K. L., Magney, T. S., Long, R. A., Vierling, L. A., Schmiege, S. C., Jennewein, J. S., Weygint, W. A., Boelman, N. T. and Bruner, S. G.: On the Functional Relationship Between Fluorescence and Photochemical Yields in Complex Evergreen Needleleaf Canopies, Geophys. Res. Lett., 47(9), 0–3, doi:10.1029/2020GL087858, 2020.

Mahadevan, P., Wofsy, S. C., Matross, D. M., Xiao, X., Dunn, A. L., Lin, J. C., Gerbig, C., Munger, J. W., Chow, V. Y. and Gottlieb, E. W.: A satellite-based biosphere parameterization for net ecosystem CO_2 exchange: Vegetation Photosynthesis and
160   Respiration Model (VPRM), Global Biogeochem. Cycles, 22(2), doi:10.1029/2006GB002735, 2008.

Marrs, J. K., Reblin, J. S., Logan, B. A., Allen, D. W., Reinmann, A. B., Bombard, D. M., Tabachnik, D. and Hutyra, L. R.: Solar-Induced Fluorescence Does Not Track Photosynthetic Carbon Assimilation Following Induced Stomatal Closure, Geophys. Res. Lett., 47(15), 0–1, doi:10.1029/2020GL087956, 2020.

Meng, L., Mao, J., Zhou, Y., Richardson, A. D., Lee, X., Thornton, P. E., Ricciuto, D. M., Li, X., Dai, Y., Shi, X. and Jia, G.: Urban warming advances spring phenology but reduces the response of phenology to temperature in the conterminous United States, Proc. Natl. Acad. Sci. U. S. A., 117(8), 4228–4233, doi:10.1073/pnas.1911117117, 2020.

Miao, G., Guan, K., Yang, X., Bernacchi, C. J., Berry, J. A., DeLucia, E. H., Wu, J., Moore, C. E., Meacham, K., Cai, Y., Peng, B., Kimm, H. and Masters, M. D.: Sun-Induced Chlorophyll Fluorescence, Photosynthesis, and Light Use Efficiency of a Soybean Field from Seasonally Continuous Measurements, J. Geophys. Res. Biogeosciences, 123(2), 610–623, doi:10.1002/2017JG004180, 2018.

Miller, J. B., Lehman, S. J., Verhulst, K. R., Miller, C. E., Duren, R. M., Yadav, V., Newman, S. and Sloop, C. D.: Large and seasonally varying biospheric CO_2 fluxes in the Los Angeles megacity revealed by atmospheric radiocarbon, Proc. Natl. Acad. Sci. U. S. A., 117(43), 26681–26687, doi:10.1073/pnas.2005253117, 2020.

Nassar, R., Napier-Linton, L., Gurney, K. R., Andres, R. J., Oda, T., Vogel, F. R. and Deng, F.: Improving the temporal and spatial distribution of CO_2 emissions from global fossil fuel emission data sets, J. Geophys. Res. Atmos., 118(2), 917–933, doi:10.1029/2012JD018196, 2013.

Oda, T., and Maksyutov, S.: ODIAC Fossil Fuel CO_2 Emissions Dataset (Version name: ODIAC2019), Center for Global Environmental Research, National Institute for Environmental Studies, doi:10.17595/20170411.001, 2015 (Reference date: 2020/04/14)

Oda, T., Maksyutov, S. and Andres, R. J.: The Open-source Data Inventory for Anthropogenic CO_2, version 2016 (ODIAC2016): a global monthly fossil fuel CO 2 gridded emissions data product for tracer transport simulations and surface flux inversions, 2, 87–107, 2018.

Oda, T., Bun, R., Kinakh, V., Topylko, P., Halushchak, M., Marland, G., Lauvaux, T., Jonas, M., Maksyutov, S., Nahorski, Z., Lesiv, M., Danylo, O. and Horabik-Pyzel, J.: Errors and uncertainties in a gridded carbon dioxide emissions inventory, Mitig. Adapt. Strateg. Glob. Chang., 24(6), 1007–1050, doi:10.1007/s11027-019-09877-2, 2019.

Olsen, S. C. and Randerson, J. T.: Differences between surface and column atmospheric CO_2 and implications for carbon cycle research, J. Geophys. Res. Atmos., 109(D2), 2004.

Pastorello, G., Papale, D., Chu, H., Trotta, C., Agarwal, D., Canfora, E., Baldocchi, D. and Torn, M.: A New Data Set to Keep a Sharper Eye on Land-Air Exchanges, Eos (Washington. DC)., (August), doi:10.1029/2017eo071597, 2017.

Pataki, D. E., Alig, R. J., Fung, A. S., Golubiewski, N. E., Kennedy, C. A., Mcpherson, E. G., Nowak, D. J., Pouyat, R. V. and Lankao, P. R.: Urban ecosystems and the North American carbon cycle, Glob. Chang. Biol., 12(11), 2092–2102, doi:10.1111/j.1365-2486.2006.01242.x, 2006.

Philip, S., Johnson, M. S., Potter, C., Genovesse, V., Baker, D. F., Haynes, K. D., Henze, D. K., Liu, J. and Poulter, B.: Prior biosphere model impact on global terrestrial CO2 fluxes estimated from OCO-2 retrievals, Atmos. Chem. Phys., 19(20), 13267–13287, doi:10.5194/acp-19-13267-2019, 2019.

Reichstein, M., Camps-Valls, G., Stevens, B., Jung, M., Denzler, J., Carvalhais, N. and Prabhat, &: Deep learning and process

understanding for data-driven Earth system science, Nature, doi:10.1038/s41586-019-0912-1, 2019.

Rolph, G., Stein, A. and Stunder, B.: Real-time environmental applications and display system: READY, Environ. Model. Softw., 95, 210–228, 2017.

200 Rosenzweig, C., Solecki, W., Romero-Lankao, P., Mehrotra, S., Dhakal, S., & Ali Ibrahim, S. Climate Change and Cities: Second Assessment Report of the Urban Climate Change Research Network. Cambridge University Press, 2018. Available on https://uccrn.ei.columbia.edu/arc3.2.

Santoro, M. and others: GlobBiomass—Global datasets of forest biomass, PANGAEA10, 1594, 2018.

Sargent, M., Barrera, Y., Nehrkorn, T., Hutyra, L. R., Gately, C. K., Jones, T., McKain, K., Sweeney, C., Hegarty, J., 205 Hardiman, B. and others: Anthropogenic and biogenic CO2 fluxes in the Boston urban region, Proc. Natl. Acad. Sci., 115(29), 7491–7496, 2018.

Schutz, B. E., Zwally, H. J., Shuman, C. A., Hancock, D. and DiMarzio, J. P.: Overview of the ICESat mission, Geophys. Res. Lett., 32(21), 1–4, doi:10.1029/2005GL024009, 2005.

Smith, I. A., Dearborn, V. K. and Hutyra, L. R.: Live fast, die young: Accelerated growth, mortality, and turnover in street 210 trees, PLoS One, 14(5), 1–17, doi:10.1371/journal.pone.0215846, 2019.

Smith, W. K., Biederman, J. A., Scott, R. L., Moore, D. J. P., He, M., Kimball, J. S., Yan, D., Hudson, A., Barnes, M. L., MacBean, N., Fox, A. M. and Litvak, M. E.: Chlorophyll Fluorescence Better Captures Seasonal and Interannual Gross Primary Productivity Dynamics Across Dryland Ecosystems of Southwestern North America, Geophys. Res. Lett., 45(2), 748–757, doi:10.1002/2017GL075922, 2018.

215 Stavros, E. N., Schimel, D., Pavlick, R., Serbin, S., Swann, A., Duncanson, L., Fisher, J. B., Fassnacht, F., Ustin, S., Dubayah, R., Schweiger, A. and Wennberg, P.: ISS observations offer insights into plant function, Nat. Ecol. Evol., 1(7), 1–4, doi:10.1038/s41559-017-0194, 2017.

Stewart, I. D. and Oke, T. R.: Local climate zones for urban temperature studies, Bull. Am. Meteorol. Soc., 93(12), 1879–1900, doi:10.1175/BAMS-D-11-00019.1, 2012.

220 Sun, Y., Frankenberg, C., Wood, J. D., Schimel, D. S., Jung, M., Guanter, L., Drewry, D. T., Verma, M., Porcar-Castell, A., Griffis, T. J., Gu, L., Magney, T. S., Kohler, P., Evans, B. and Yuen, K.: OCO-2 advances photosynthesis observation from space via solar- induced chlorophyll fluorescence, Science (80-.)., 358(6360), aam5747, doi:10.1126/science.aam5747, 2017.

Van Der Tol, C., Verhoef, W., Timmermans, J., Verhoef, A. and Su, Z.: An integrated model of soil-canopy spectral radiances, photosynthesis, fluorescence, temperature and energy balance, Biogeosciences, 6(12), 3109–3129, doi:10.5194/bg-6-3109-225 2009, 2009.

Tramontana, G., Jung, M., Schwalm, C. R., Ichii, K., Camps-Valls, G., Ráduly, B., Reichstein, M., Arain, M. A., Cescatti, A., Kiely, G., Merbold, L., Serrano-Ortiz, P., Sickert, S., Wolf, S. and Papale, D.: Predicting carbon dioxide and energy fluxes across global FLUXNET sites with regression algorithms, Biogeosciences, 13(14), 4291–4313, doi:10.5194/bg-13-4291-2016, 2016.

230 Turnbull, J. C., Sweeney, C., Karion, A., Newberger, T., Lehman, S. J., Tans, P. P., Davis, K. J., Lauvaux, T., Miles, N. L.,

Richardson, S. J., Cambaliza, M. O., Shepson, P. B., Gurney, K., Patarasuk, R. and Razlivanov, I.: Toward quantification and source sector identification of fossil fuel CO_2 emissions from an urban area: Results from the INFLUX experiment, J. Geophys. Res., 120(1), 292–312, doi:10.1002/2014JD022555, 2015.

235 Turner, A. J., Köhler, P., Magney, T. S., Frankenberg, C., Fung, I. and Cohen, R. C.: A double peak in the seasonality of California's photosynthesis as observed from space, Biogeosciences, 17(2), 405–422, doi:10.5194/bg-17-405-2020, 2020.

Turner, A. J., Köhler, P., Magney, T. S., Frankenberg, C., Fung, I., and Cohen, R. C.: Extreme events driving year-to-year differences in gross primary productivity across the US, Biogeosciences Discuss, doi:10.5194/bg-2021-49, in review, 2021.

Verma, M., Schimel, D., Evans, B., Frankenberg, C., Beringer, J., Drewry, D. T., Magney, T., Marang, I., Hutley, L., Moore, C. and Eldering, A.: Effect of environmental conditions on the relationship between solar-induced fluorescence and gross
240 primary productivity at an OzFlux grassland site, J. Geophys. Res. Biogeosciences, 122(3), 716–733, doi:10.1002/2016JG003580, 2017.

Vahmani, P. and Hogue, T. S.: Incorporating an Urban Irrigation Module into the Noah Land Surface Model Coupled with an Urban Canopy Model, J. Hydrometeorol., 15(4), 1440–1456, doi:10.1175/jhm-d-13-0121.1, 2014.

Vasenev, V. and Kuzyakov, Y.: Urban soils as hot spots of anthropogenic carbon accumulation: Review of stocks, mechanisms
245 and driving factors, L. Degrad. Dev., 29(6), 1607–1622, 2018.

Wang, S., Ju, W., Peñuelas, J., Cescatti, A., Zhou, Y., Fu, Y., Huete, A., Liu, M. and Zhang, Y.: Urban−rural gradients reveal joint control of elevated CO_2 and temperature on extended photosynthetic seasons, Nat. Ecol. Evol., doi:10.1038/s41559-019-0931-1, 2019.

Wen, J., Köhler, P., Duveiller, G., Parazoo, N. C., Magney, T. S., Hooker, G., Yu, L., Chang, C. Y. and Sun, Y.: A framework
250 for harmonizing multiple satellite instruments to generate a long-term global high spatial-resolution solar-induced chlorophyll fluorescence (SIF), Remote Sens. Environ., 239(January), doi:10.1016/j.rse.2020.111644, 2020.

White, E. D., Rigby, M., Lunt, M. F., Luke Smallman, T., Comyn-Platt, E., Manning, A. J., Ganesan, A. L., O'Doherty, S., Stavert, A. R., Stanley, K., Williams, M., Levy, P., Ramonet, M., Forster, G. L., Manning, A. C. and Palmer, P. I.: Quantifying the UK's carbon dioxide flux: An atmospheric inverse modelling approach using a regional measurement network, Atmos.
255 Chem. Phys., 19(7), 4345–4365, doi:10.5194/acp-19-4345-2019, 2019.

Wohlfahrt, G., Gerdel, K., Migliavacca, M., Rotenberg, E., Tatarinov, F., Müller, J., Hammerle, A., Julitta, T., Spielmann, F. M. and Yakir, D.: Sun-induced fluorescence and gross primary productivity during a heat wave, Sci. Rep., 8(1), 1–9, doi:10.1038/s41598-018-32602-z, 2018.

Wu, D., Lin, J. C., Fasoli, B., Oda, T., Ye, X., Lauvaux, T., Yang, E. G., and Kort, E. A.: A Lagrangian approach towards
260 extracting signals of urban CO_2 emissions from satellite observations of atmospheric column CO_2 (XCO₂): X-Stochastic Time-Inverted Lagrangian Transport model ("X-STILT v1"), Geosci. Model Dev., 11, 4843–4871, doi:10.5194/gmd-11-4843-2018, 2018.

Wu, K.: Joint Estimation of Fossil Fuel and Biogenic CO_2 Fluxes in an Urban Environment [unpublished] Doctor of Philosophy Dissertation, 2020a, https://etda.libraries.psu.edu/catalog/17434kzw151, Accessed 2020-09-01.

265 Wu, D.: Solar-Induced Fluorescence for Modeling Urban biogenic Fluxes (SMUrFv1), 2020b, doi:10.5281/zenodo.4018123,

https://zenodo.org/record/4018124#.X3O1DpNKioo, Accessed 2021-04-09.

Xia, Y., Mitchell, K., Ek, M., Sheffield, J., Cosgrove, B., Wood, E., Luo, L., Alonge, C., Wei, H., Meng, J., Livneh, B., Lettenmaier, D., Koren, V., Duan, Q., Mo, K., Fan, Y. and Mocko, D.: Continental-scale water and energy flux analysis and validation for the North American Land Data Assimilation System project phase 2 (NLDAS-2): 1. Intercomparison and application of model products, J. Geophys. Res. Atmos., 117(3), doi:10.1029/2011JD016048, 2012.

Xiao, J., Davis, K. J., Urban, N. M. and Keller, K.: Uncertainty in model parameters and regional carbon fluxes: A model-data fusion approach, Agric. For. Meteorol., 189–190, 175–186, doi:10.1016/j.agrformet.2014.01.022, 2014.

Yang, J., Chang, Y. and Yan, P.: Ranking the suitability of common urban tree species for controlling PM2.5 pollution, Atmos. Pollut. Res., 6(2), 267–277, doi:10.5094/APR.2015.031, 2015a.

Yang, K., Ryu, Y., Dechant, B., Berry, J. A., Hwang, Y., Jiang, C., Kang, M., Kim, J., Kimm, H., Kornfeld, A. and Yang, X.: Sun-induced chlorophyll fluorescence is more strongly related to absorbed light than to photosynthesis at half-hourly resolution in a rice paddy, Remote Sens. Environ., 216(June), 658–673, doi:10.1016/j.rse.2018.07.008, 2018.

Yang, X., Tang, J., Mustard, J. F., Lee, J. E., Rossini, M., Joiner, J., Munger, J. W., Kornfeld, A. and Richardson, A. D.: Solar-induced chlorophyll fluorescence that correlates with canopy photosynthesis on diurnal and seasonal scales in a temperate deciduous forest, Geophys. Res. Lett., 42(8), 2977–2987, doi:10.1002/2015GL063201, 2015b.

Ye, X., Lauvaux, T., Kort, E. A., Oda, T., Feng, S., Lin, J. C., Yang, E. G. and Wu, D.: Constraining fossil fuel CO_2 emissions from urban area using OCO-2 observations of total column CO_2, J. Geophys. Res. Atmos., e2019JD030528, doi:10.1029/2019jd030528, 2020.

Yin, Y., Byrne, B., Liu, J., Wennberg, P. O. and Davis, K. J.: Cropland Carbon Uptake Delayed and Reduced by 2019 Midwest Floods, 1–15, doi:10.1029/2019AV000140, 2020.

You, L., Wood, S., Wood-Sichra, U. and Wu, W.: Generating global crop distribution maps: From census to grid, Agric. Syst., 127, 53–60, doi:10.1016/j.agsy.2014.01.002, 2014.

Zhang, Y., Joiner, J., Alemohammad, S. H., Zhou, S., Gentine, P., Hamed Alemohammad, S., Zhou, S. and Gentine, P.: A global spatially contiguous solar-induced fluorescence (CSIF) dataset using neural networks, Biogeosciences, 15(19), 5779–5800, doi:10.5194/bg-2018-255, 2018.

Zhao, Z., Peng, C., Yang, Q., Meng, F. R., Song, X., Chen, S., Epule, T. E., Li, P. and Zhu, Q.: Model prediction of biome-specific global soil respiration from 1960 to 2012, Earth's Futur., 5(7), 715–729, doi:10.1002/2016EF000480, 2017.

Zuromski, L. M., Bowling, D. R., Köhler, P., Frankenberg, C., Goulden, M. L., Blanken, P. D. and Lin, J. C.: Solar-Induced Fluorescence Detects Interannual Variation in Gross Primary Production of Coniferous Forests in the Western United States, Geophys. Res. Lett., 45(14), 7184–7193, 2018.
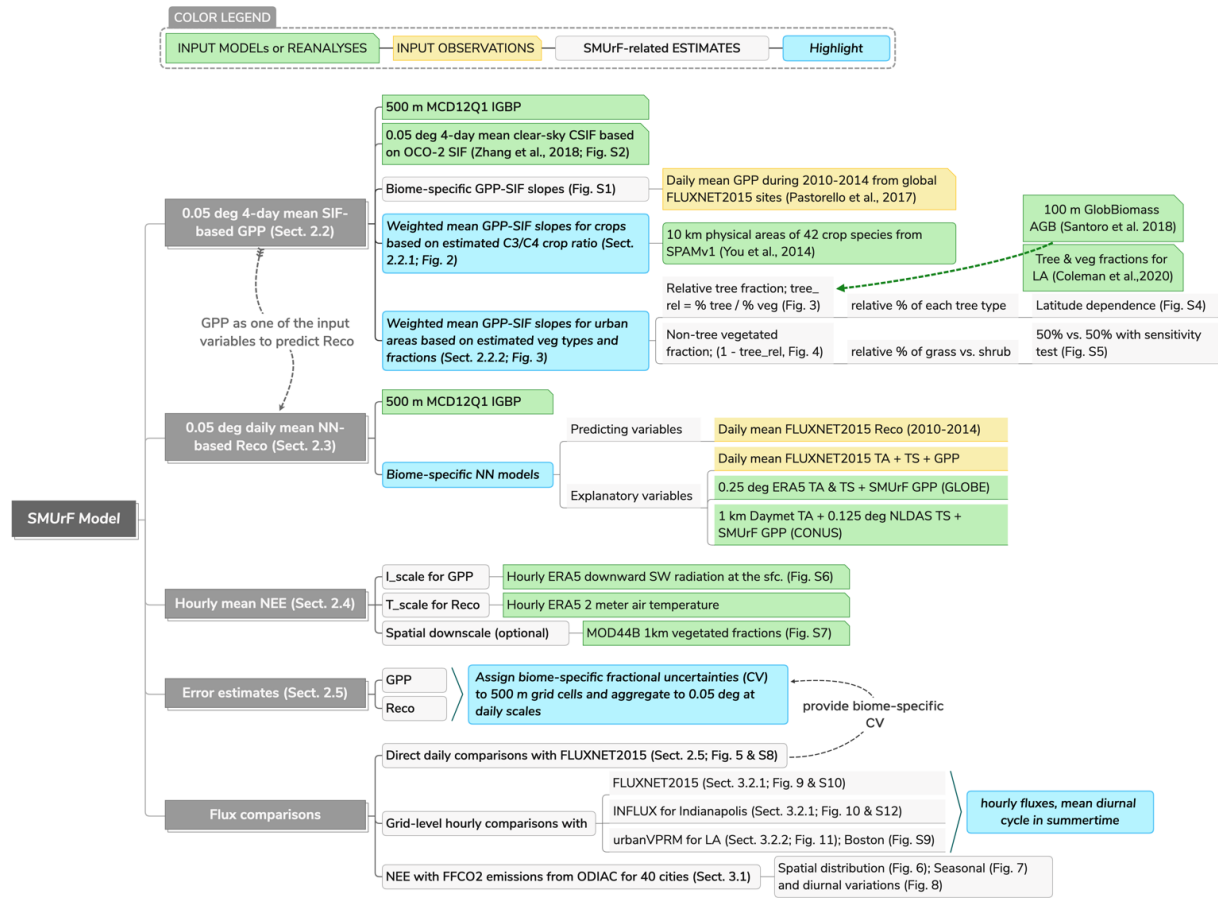
Product Name		Spatial Info	Temporal Info	Usage
MODIS MCD12Q1V6 IGBP		500 m, global	Annual mean, 2010-2018	Provide biome types
CSIF		0.05°, global	4-day mean, 2000-2018	Estimate 4-day mean GPP
FLUXNET2015		Global sites	Daily data from 2010-2014	Calculate GPP-SIF slopes and train R_{eco}
MAPSPAMV1 (physical crop areas)		10 km, global	Annual mean for 2010	Estimate global C3/C4 crop ratios
GlobBiomass (above ground biomass)		100 m, global	Annual mean for 2010	Estimate tree fractions in cities
NAIP-based land cover classification		0.6 m, LA		For deriving AGB-tree fraction relationship
ERA5	air and soil temperature (2T, STL1)	0.25°, global	Daily mean, 2010-2018	Predict R_{eco} for the entire globe
	shortwave radiation (SSRD)		Hourly mean, 2010-2018	Hourly downscaling
Daymet (air temperature)		1 km, CONUS	Hourly mean, 2010-2018	Predict R_{eco} for CONUS
NLDAS (soil temperature)		0.125°, CONUS	Hourly mean, 2010-2018	
SMURF		0.05°	Hourly mean, 2010-2018	Provide biospheric fluxes for cities

300

Figure 1. A demonstration of SMUrF (flow chart) and description of input data products and observations summarized in the table below. The temporal coverage in the table indicates the years used in this study.
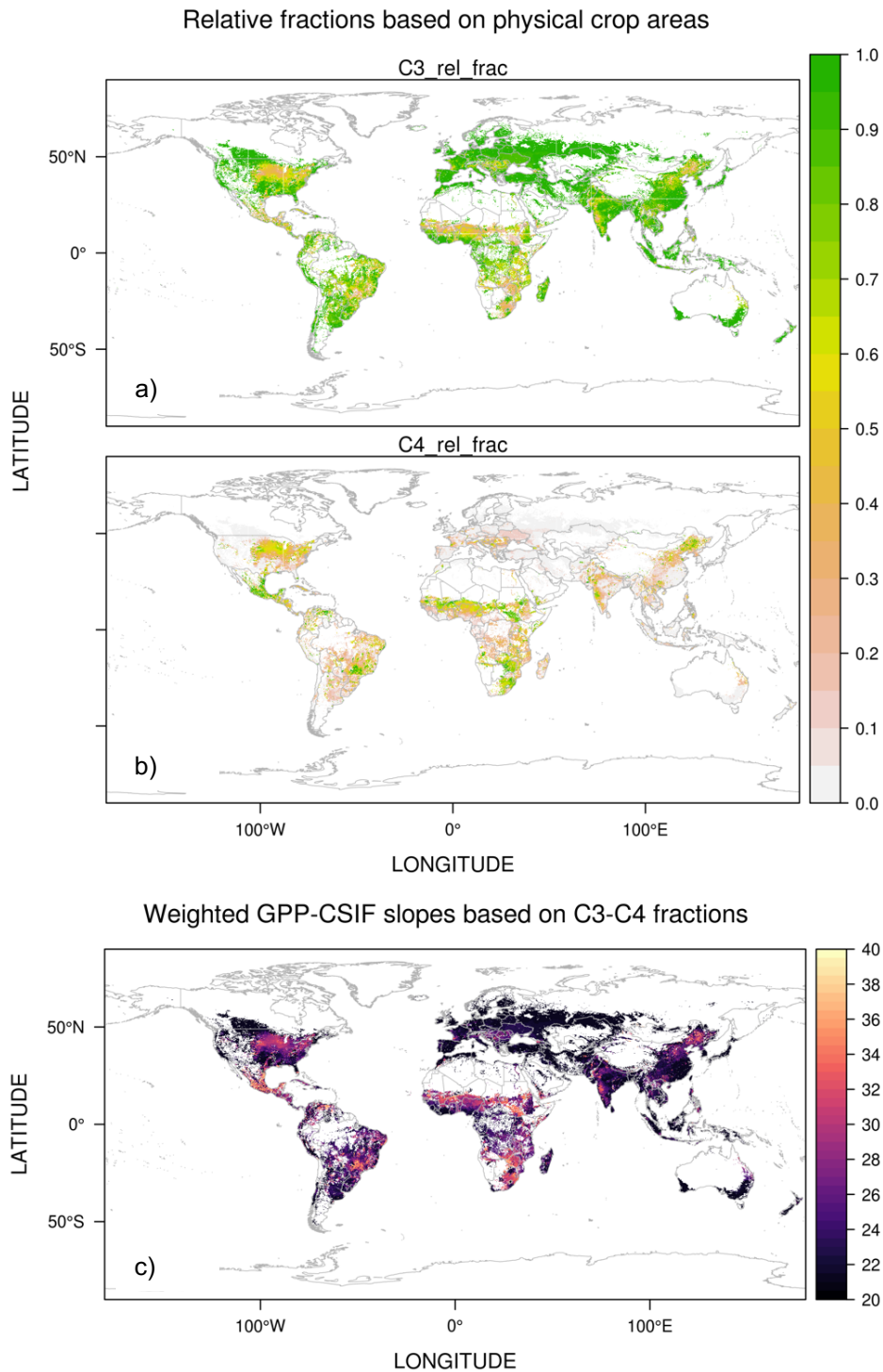
Figure 2. Spatial distribution of the estimated C3:C4 ratio [%] (a-b) using physical areas of 42 crop species from MapSPAMv1 and weighted mean GPP-CSIF slopes [(μmol m^{-2} s^{-1}) / (mW m^{-2} nm^{-1} sr^{-1}] for croplands (c).
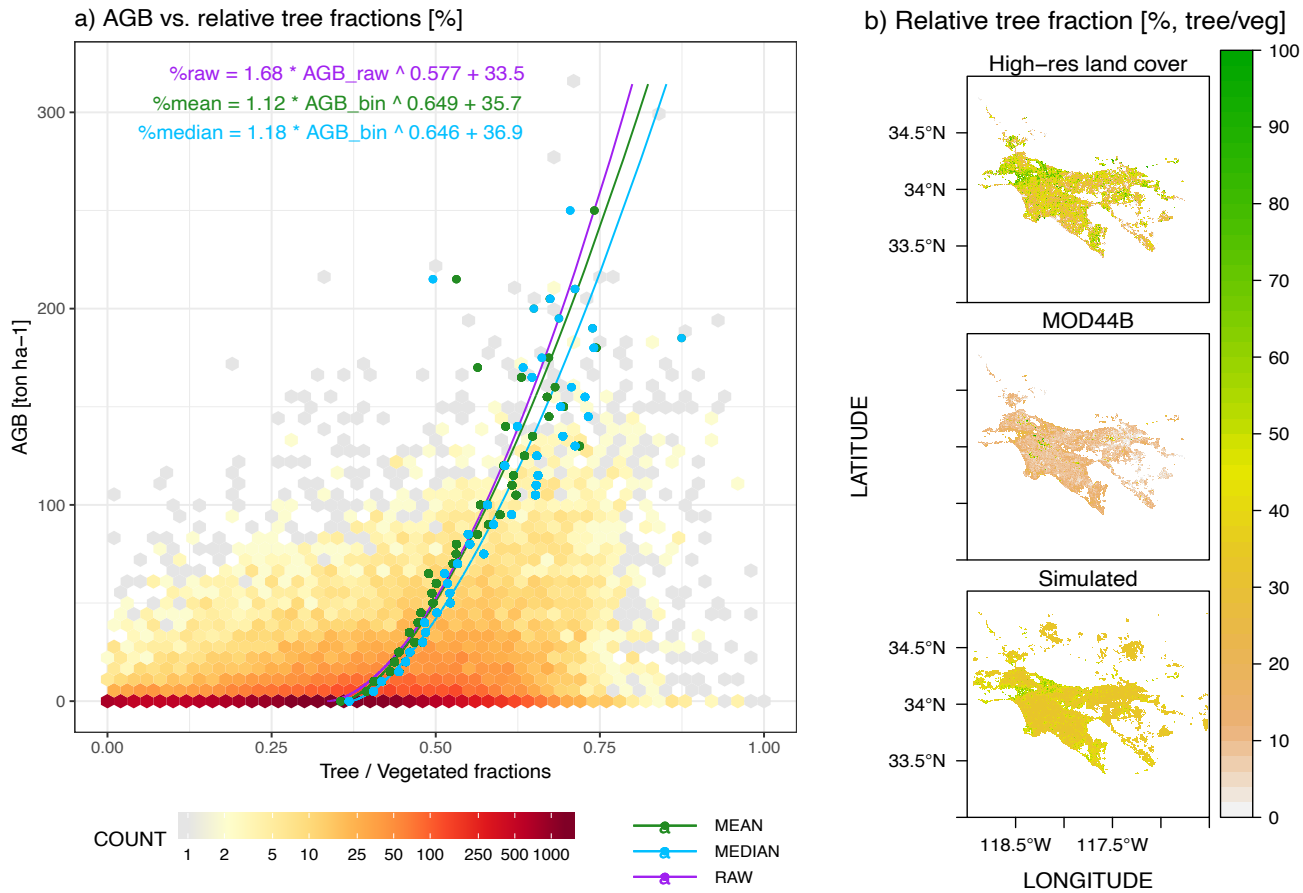
Figure 3. a) Power law relationships fitted between the above ground biomass (AGB) and raw relative tree fractions (purple line) as well as fits using binned AGB and mean/median relative tree fractions per AGB bin (green/blue lines). The statistical fit in purple is chosen to predict relative tree fractions within cities. **b)** Spatial distributions of calculated relative tree fractions (%) from a high-resolution NAIP-based land cover classification product (Coleman et al., 2020) (top panel), Vegetation Continuous Fields from MOD44B v6 product (middle panel), and our approximation (bottom panel) using AGB and the statistical fit illustrated in panel a).
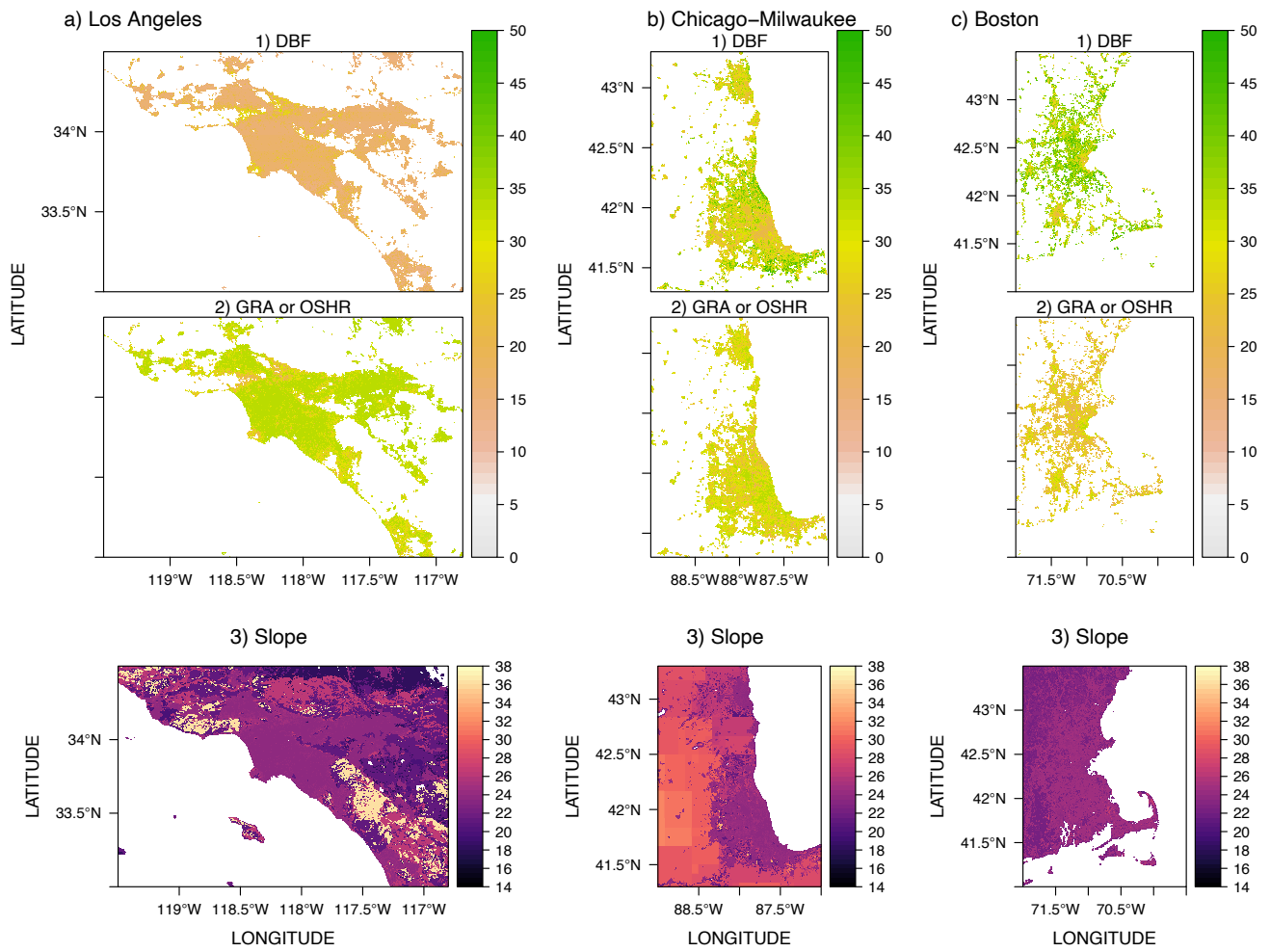
Figure 4. Estimated relative deciduous broadleaf forest (DBF, 1st row) and non-tree fractions ($f_{non\text{-}tree}$, 2nd row) at 500 m and GPP-SIF slopes after urban gap-fills (3rd row) for Los Angeles (a), Chicago (b), and Boston (c).
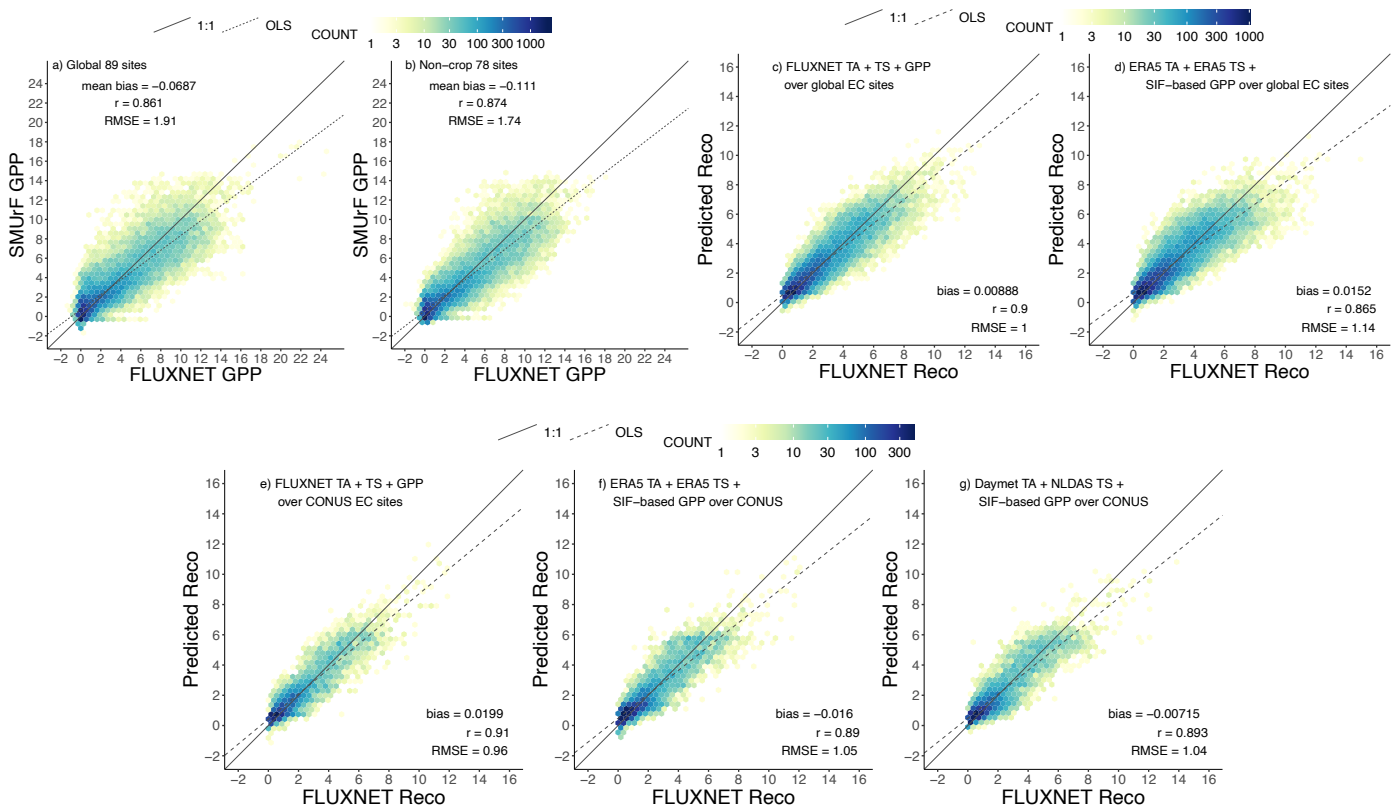
Figure 5. Comparisons between directly computed fluxes from SMUrF and observed fluxes from FLUXNET during 2010 – 2014 as density plots with 50 bins. All fluxes have units of μmol m^{-2} s^{-1}. **a-b)** 4-day mean observed GPP and directly computed SIF-based GPP at 89 global EC sites (a) and 78 non-crop sites (b). **c-d)** An evaluation of the daily mean observed R_{eco} and predicted R_{eco} on the testing set (i.e., 20% of all data) using observed T_{air} + T_{soil} + GPP from FLUXNET (c) OR T_{air} + T_{soil} from ERA5 and SIF-based GPP (d) for 89 global EC sites.

e-g) Similar to panels **c-d,** but model-data R_{eco} comparison ONLY for US EC sites and modeled R_{eco} is calculated using Daymet T_{air}, NLDAS T_{soil}, and SIF-based GPP (g). Although GPP and R_{eco} were trained and predicted separately per biome, model-data pairs from all biomes are collected for visualization purpose. For each panel, numbers of data points in each of the 50 bins are displayed in log$_{10}$ scales as yellow-blue colours and error statistics including mean bias, correlation coefficient, and RMSE are printed. 1:1 and OLS-based regression lines are displayed in solid and dashed lines. RMSEs derived from these direct validations were further used for assigning uncertainties at 500 m grid cell (**Sect. 2.5**).
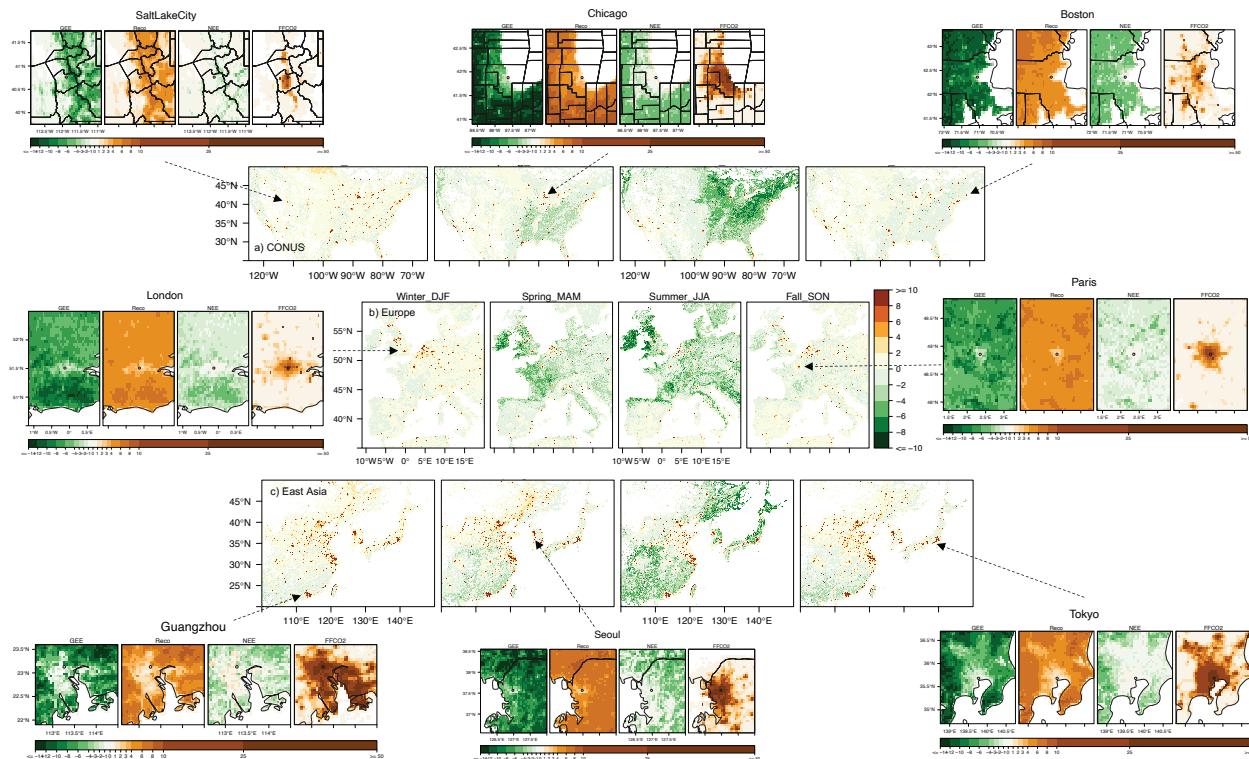
Figure 6. The sums of seasonal mean SMUrF-based NEE and ODIAC-based FFCO$_2$ [μmole m^{-2} s^{-1}] for CONUS (a), western Europe (b), and East Asia (c) at 0.05º for 2018. Spatial distributions of the average GEE (= -GPP), R$_{eco}$, NEE, and FFCO$_2$ from ODIAC over JJA 2018 are provided for 8 cities (hereinafter zoomed-in panels). As an optional step, these fluxes can further be spatially downscaled to 1 km using MOD44B (**Fig. S7**).
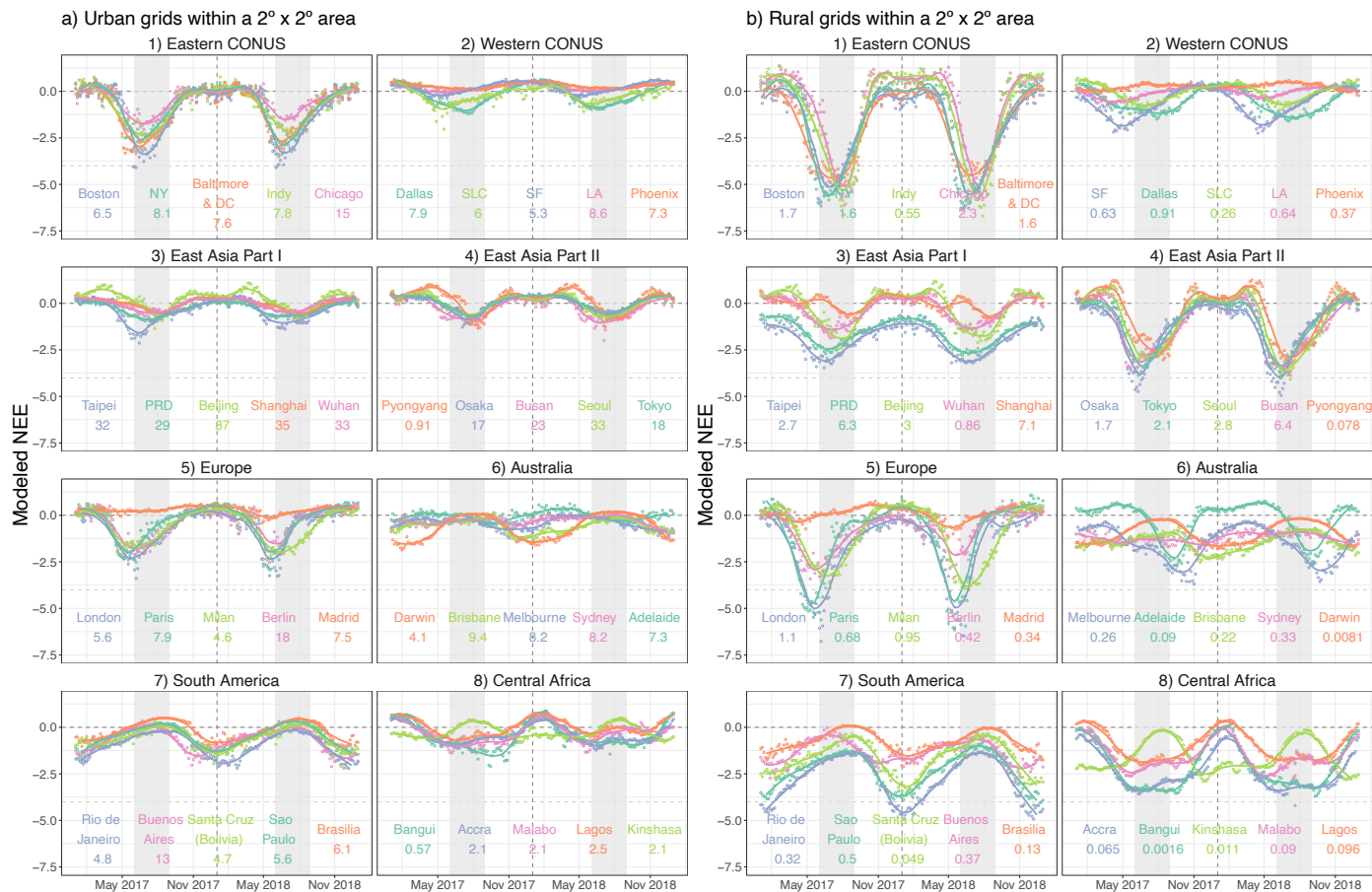
Figure 7. A multi-city comparison of the spatially average NEE fluxes [μmol m^{-2} s^{-1}] over urban **(a)** and rural **(b)** grid cells within a 2° × 2° area around the urban center for 2017 – 2018. We present the 4-day mean (in circles) and monthly mean (smoothed splines) NEE for 40 selected cities in CONUS, western Europe, east Asia, eastern Australia, south America, and central Africa. Light grey ribbons indicate the typical north hemispheric summer months (June-Aug, JJA). The numbers below city names denote the spatially average fossil fuel CO_2 emissions derived from ODIAC over the same grid cells as NEE.

Figure 8. A multi-city comparison of the average diurnal cycles of SMUrF-derived NEE fluxes (triangles and solid lines) and ODIAC-TIMES based FFCO₂ (solid dots) [μmol m^{-2} s^{-1}] over JJA 2018 over the urban **(a)** and rural **(b)** grid cells within a 2° × 2° area around each urban center. *** Note that the y-scales of positive and negative fluxes are different for panel a) to better reveal the NEE fluxes, i.e., 0 to 60 μmol m^{-2} s^{-1} for positive fluxes and -20 to 0 μmol m^{-2} s^{-1} for negative fluxes. Light grey ribbons indicate the negative flux ranges from -10 to 0 μmol m^{-2} s^{-1} while light-yellow ribbons indicate the positive flux ranges from 0 to +10 μmol m^{-2} s^{-1}. City names are labelled on the bottom of each panel.

Density plot of hourly mean NEE per biome for 67 EC sites in US and EU from 2010–2014
with 1:1 line (solid) and OLS fit (dashed)
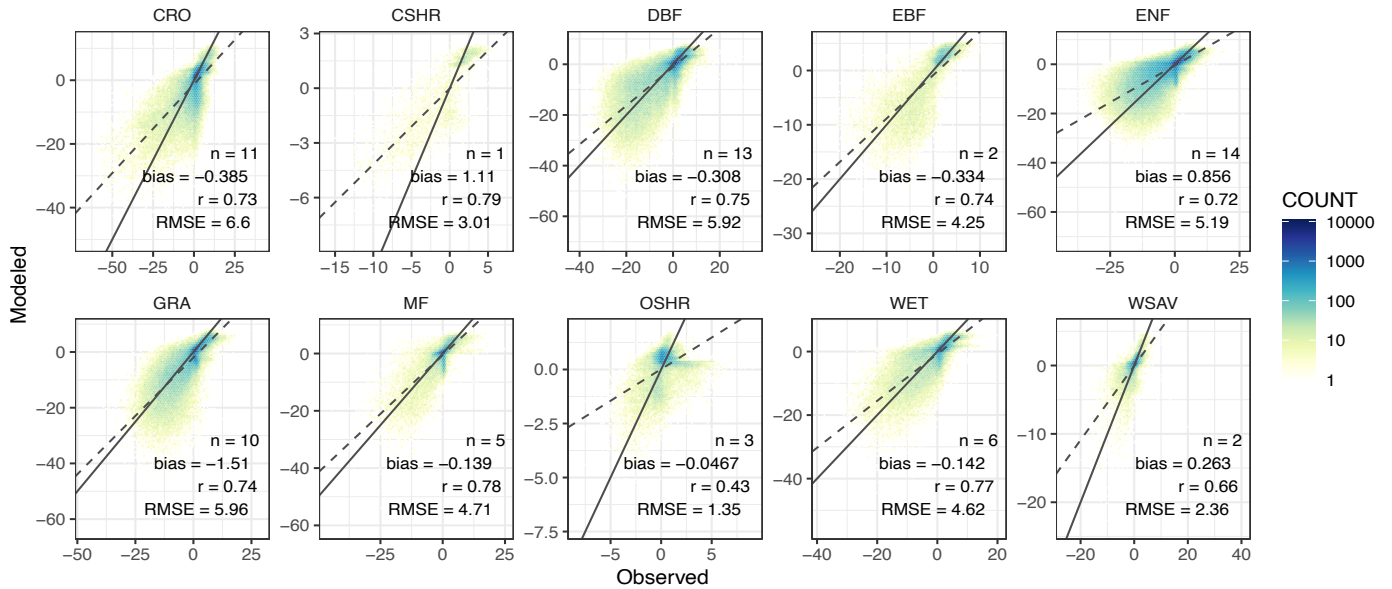
Figure 9. Hourly flux comparisons between modeled NEE against measured NEE from FLUXNET are presented in density plot for each biome. The number of EC sites per biome (n) and several error statistics including the mean bias, correlation coefficient (r), and root-mean-square error (RMSE) are printed on the bottom right corner of each panel.
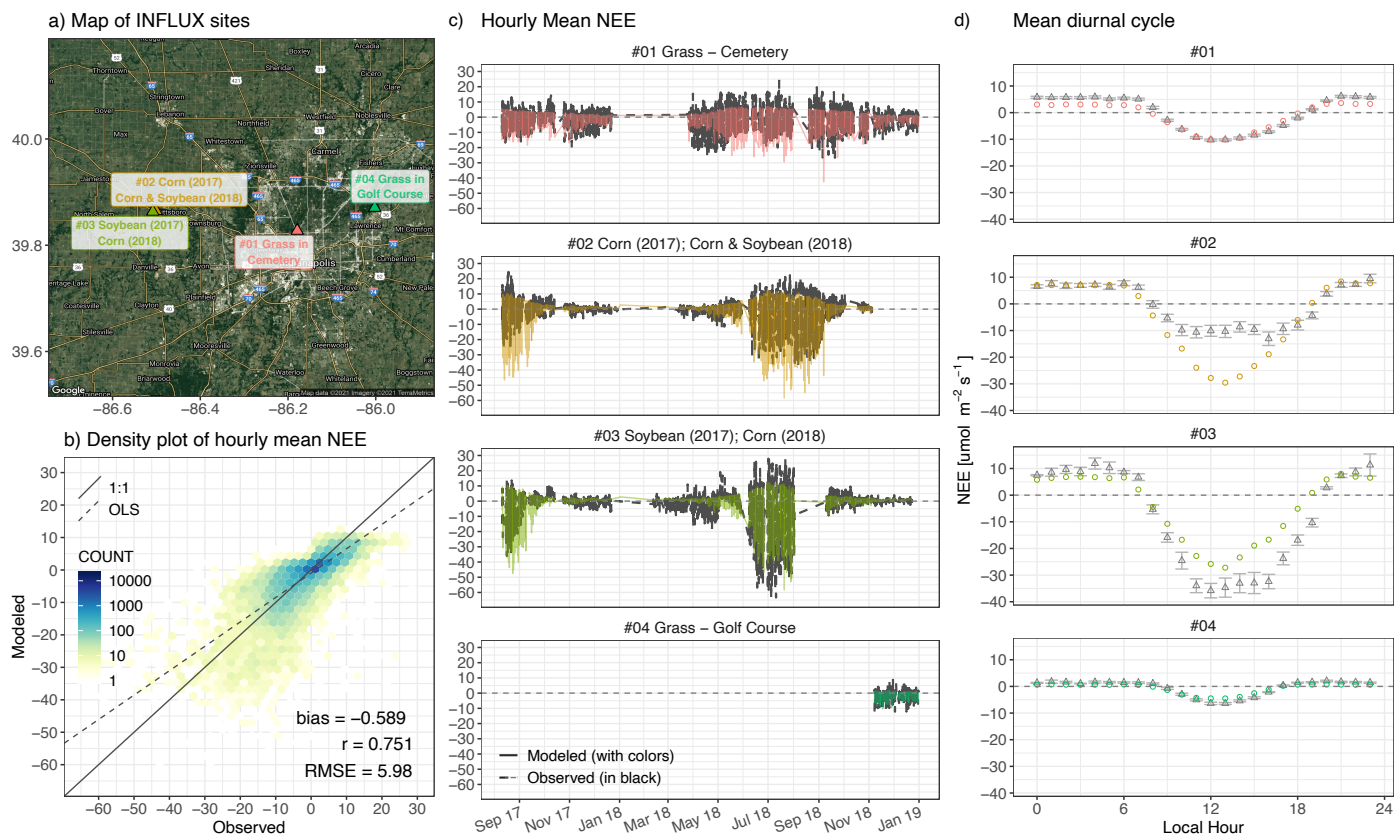
Figure 10. NEE flux evaluation based on four EC towers from the INFLUX network around Indianapolis (**a**). Model-data flux comparisons at the hourly scale [μmol m^{-2} s^{-1}] from August 2017 to December 2018 are shown as density plot (**b**) and time series (**c**). Error statistics in hourly NEE including the mean bias, correlation coefficient (r), and root-mean-square error (RMSE) are printed on the bottom right corner of panel b). **d)** Mean diurnal cycle of observed NEE (black triangles) and modeled NEE (coloured circles) over JJA for two cropland sites (sites #2 and #3) and the entire year of 2018 for urban vegetation sites (sites #1 and #4). For panel c and d, Model fluxes are shown in solid lines or circles with four colours indicating different sites, whereas measured fluxes are shown in black dashed lines or triangles. Supplementary information on the spatial map of modeled NEE and monthly mean NEE comparisons can be found in **Fig. S12**.
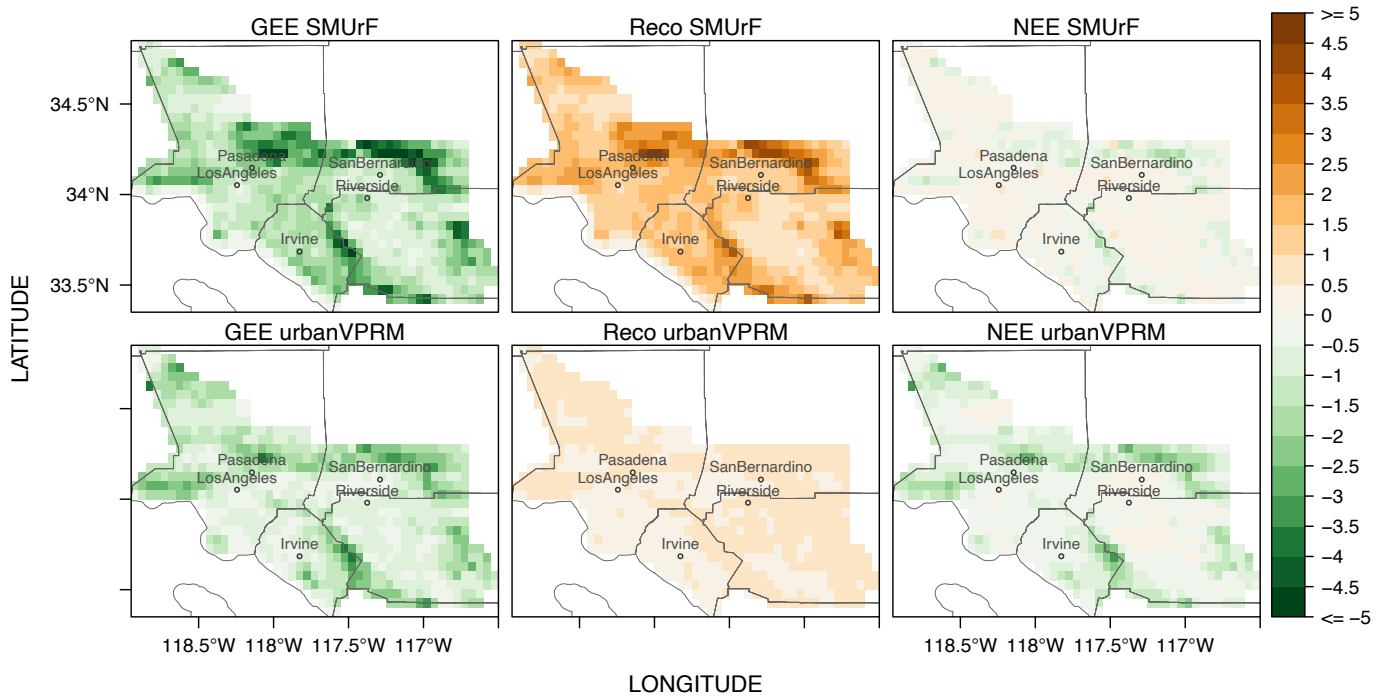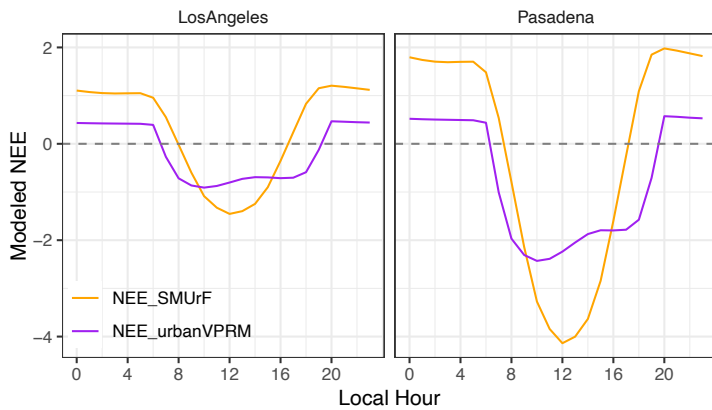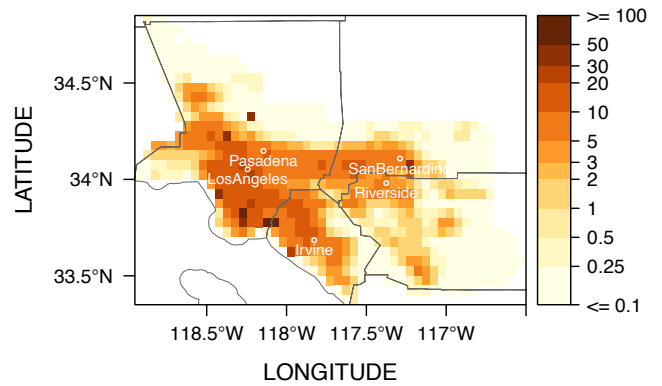
Figure 11. a) Spatial maps of mean GEE, R_{eco}, and NEE fluxes [μmol m^{-2} s^{-1}] from SMUrF and urbanVPRM over the greater Los Angeles region from July to September (JAS) in 2017. **b)** Mean diurnal cycles of NEE fluxes over JAS 2017 between two models. **c)** Map of mean FFCO$_2$ [μmol m^{-2} s^{-1}] at 0.05° aggregated from 1 km ODIAC product over JAS 2017. Main cities have been labelled on the maps including Los Angeles, Pasadena, Irvine, Riverside, and San Bernardino.
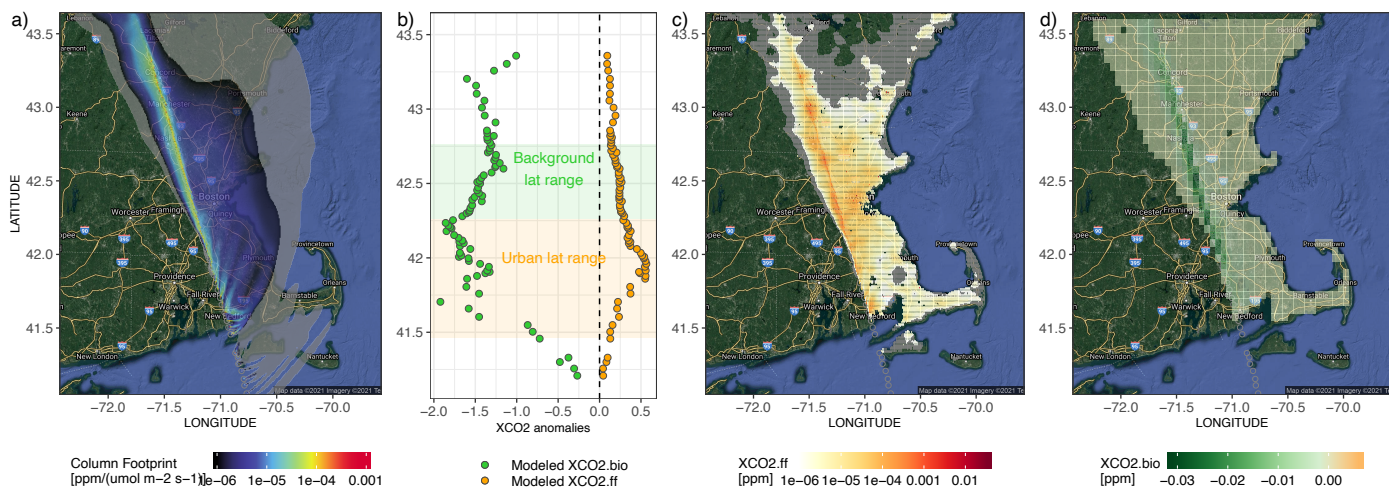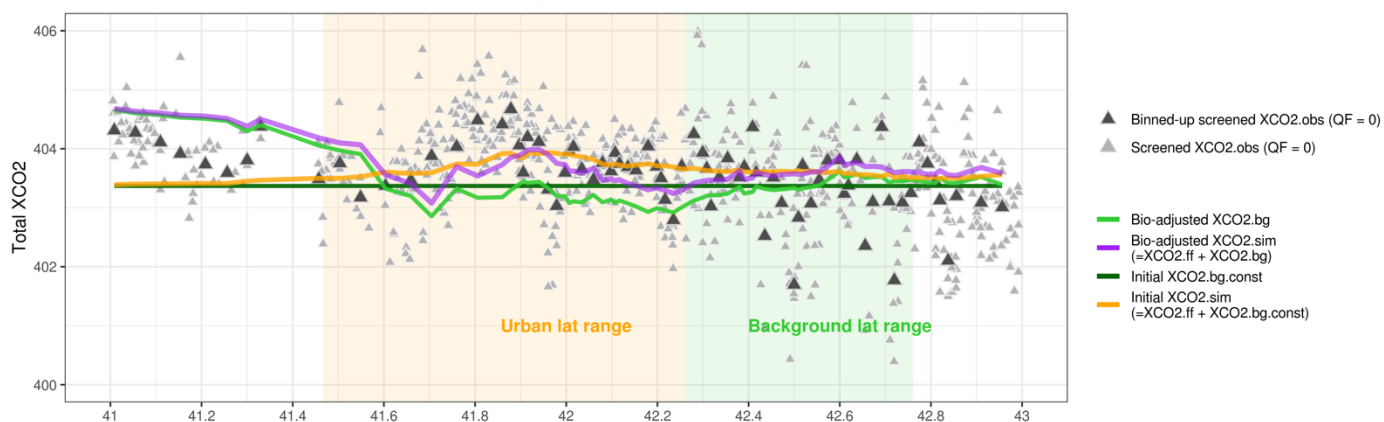
Figure 12. Demonstration of the application of SMUrF in the context of column CO_2 measurements for an OCO-2 overpass on 1700UTC 7th July 2018 to the west of Boston. The time-integrated column footprints [ppm / (μmol m^{-2} s^{-1})] originated from dozens of receptor locations have been integrated along the latitude (**a**). The wind was blowing from the urban center of Boston onto the satellite swath. **c-d)** Spatially-explicit XCO_2 contributions from ODIAC-based FFCO$_2$ and SMUrF-based NEE ($XCO_{2.ff}$ and $XCO_{2.bio}$ in ppm). Note that spatial footprint (**panel a**) and the spatial contribution of $XCO_{2.ff}$ (**panel c**) are plotted in log$_{10}$ scale with small values < 10^{-6} ppm / (μmol m^{-2} s^{-1}) displayed in light grey. The upwind contributions with respect to a column receptor are summed up, which arrive at the total modeled $XCO_{2.ff}$ or $XCO_{2.bio}$ anomalies per receptor (orange or green dots in panel **b**). Light orange and green ribbons indicate the urban-enhanced and background latitude range, following the approach in Wu et al. (2018) (also demonstrated in **Fig S13**).

e) An example of incorporating $\Delta XCO_{2.bio}$ into the background estimates. The screened observed XCO_2 (QF = 0; gray triangles) are averaged in bins to match the locations of X-STILT receptors (black triangles). The dark and light green lines imply the constant and the bio-adjusted XCO_2 background. Differences between two $XCO_{2.bg}$ indicate the $\Delta XCO_{2.bio}$, which is calculated by subtracting the mean $XCO_{2.bio}$ within the rural range from all the simulated $XCO_{2.bio}$ along the swath. The FFCO$_2$ enhancements are further added to the two different background values to arrive at the total modeled XCO_2 (orange and purple lines).
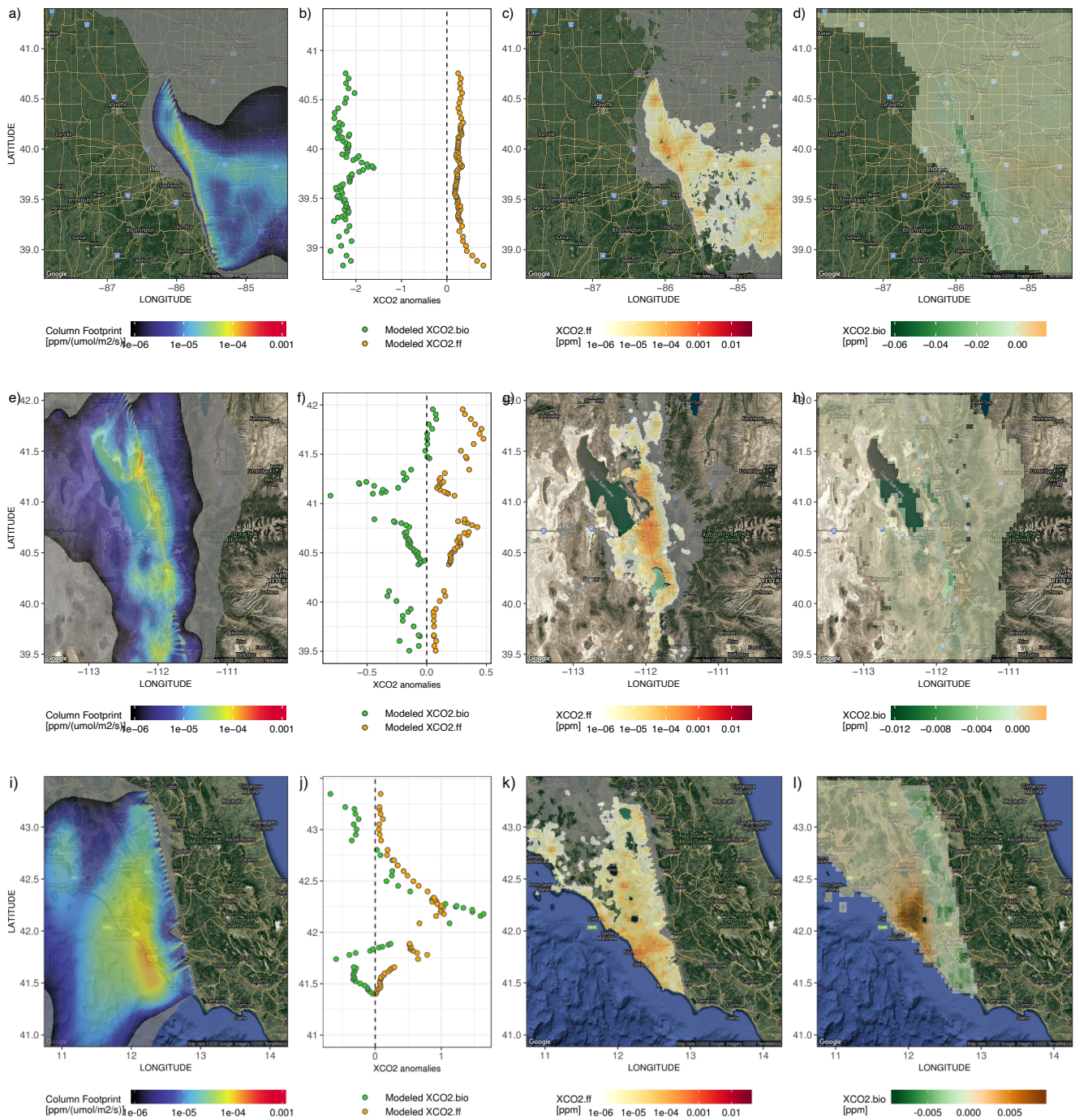
Figure 13. Similar to **Figure 12a-d**, but for three different OCO-2 tracks, including 1800UTC 13th July 2018 to the east of Indianapolis (2018071318; 1st row, **a-d**), 2000UTC 25th June 2018 right over Salt Lake City (2018062520; 2nd row, **e-h**), and 1200UTC 15th June 2017 near Rome, Italy (2017061512; 3rd row, **i-l**). Meteorological fields that drove those simulations are 3km HRRR for US cities and 0.5degree GDAS fields for Rome.